

4192

MULTICHANNEL SURFACE DISCHARGE SWITCHES

MULTICHANNEL SURFACE DISCHARGE SWITCHES

BY

W. J. IP, B.Eng.

A Project Report

Submitted to the School of Graduate Studies

in Partial Fulfilment of the Requirements

for the degree

Master of Engineering

McMaster University

April 1981

MASTER OF ENGINEERING (1981)

McMASTER UNIVERSITY

Engineering Physics

HAMILTON, ONTARIO

TITLE: Multichannel Surface Discharge Switches *Part B*
AUTHOR: Wai-Ting Joseph Ip, B.Eng. (McMaster University)
SUPERVISOR: Dr. S.T. Pai
NO. OF PAGES: x,74

ABSTRACT

High pressure surface discharge switches have become the subject of applied research in recent years due to their important application in pulse power systems. The purpose of this study is to gain a better understanding of the subject so that an optimum design of the switch may be achieved. The surface discharge phenomena is examined under single channel static breakdown condition to attempt to isolate individual processes involved. The multi-channel switch developed by the NRC is tested with a resistive load assembly to determine the optimum operating conditions. The lifetime characteristic is also studied using a small experimental device. Finally, two models for the switch are developed to fit the observed data.

ACKNOWLEDGEMENTS

The author would like to sincerely thank Dr. S.T. Pai for his helpful suggestions and supervision of this project. The author also wishes to thank Dr. J.P. Marton and his colleagues at Opto-Electronics Ltd. for their valuable assistance during the course of this work.

Finally, the author wishes to express his regards to his parents who have given him constant encouragement and moral support throughout these years.

TABLE OF CONTENTS

	PAGE
LIST OF ILLUSTRATIONS	vii
LIST OF TABLES	ix
GLOSSARY OF SYMBOLS	x
CHAPTER 1 INTRODUCTION	1
1.1 Pulse Power Switch Requirements	1
1.2 Multichannel Surface Spark Gap	2
1.3 General Outline of the Study	3
CHAPTER 2 STATIC BREAKDOWN EXPERIMENTS	7
2.1 Physical Processes Involved in Surface Discharge	7
2.2 Experiments and Results	8
2.3 Discussion	16
CHAPTER 3 HIGH-VOLTAGE PULSE BREAKDOWN EXPERIMENTS	19
3.1 Resistive Load Test Assembly	19
3.2 Monitoring System	22
3.3 High-Voltage Measurement Techniques	23

	PAGE
3.4 Switch Performance	26
3.5 Life Testing	36
CHAPTER 4 MODELING OF SWITCH	43
4.1 Engineering Model	43
4.2 Physical Model	50
CHAPTER 5 CONCLUSIONS	61
5.1 Summary of Results	61
5.2 Suggestions for Future Investigation	63
APPENDIX A LIST OF EQUIPMENT	65
APPENDIX B NUMERICAL METHODS	66
APPENDIX C COMPUTER PROGRAM LISTING	68
REFERENCES	72

LIST OF ILLUSTRATIONS

FIGURE		PAGE
1.	NRC Multichannel Surface Spark Gap Design	5
2.	Cross-Sectional View of Experimental Switch	6
3.	(a-f) Field Distortion Effects	9
4.	Deviation From Static Air Breakdown Field As a Function of r	11
5.	(a) E_s as a Function of Dielectric Constant	14
	(b) r_B as a Function of Dielectric Constant	14
6.	(a) E_s as a Function of Surface Resisitivity	15
	(b) r_B as a Function of Surface Resisitivity	15
7.	Schematic Representation of the Resistive Load Test Assembly	21
8.	Complete System Layout Utilizing the ' Tree Wiring Method '	25
9.	(a) Effect of V_0 on V_m for Different P's	28
	(b) Effect of V_0 on t_r for Different P's	29
10.	Effect of P on V_m for Different SSG Pressures	30
11.	t_r Versus V_m	31
12.	t_r^2 Versus $1/V_m$	32

FIGURE	PAGE
13. Effect of V_0 on N for Different P's	33
14. (a) Voltage and Current as a Function of Time	37
(b) Impedence as a Function of Time	37
15. A Typical Light Pulse	41
16. (a) Voltage Waveform	41
(b) Current Waveform	41
(c) Light Pulse Waveform	41
17. N Versus r	42
18. (a) Equivalent Circuit of Resistive Load Test Assembly	47
(b) Assumed Time Functions for R_2 and L_2	47
19. (a,b) Effects of L_0 on Voltage and Current	48
20. (a,b) Effects of τ_L on Voltage and Current	49
21. (a-c) Pre-Spark Characteristics	52
22. Notations used in Derivation of Model	56
23. Jitter Time as a Function of Holdoff Voltage	56

LIST OF TABLES

TABLE	PAGE
1. Life Testing Results	42

GLOSSARY OF SYMBOLS

d	Electrode separation.
r	Electrode-substrate separation.
E_0	Static breakdown field in air (without substrate).
E_s	Static breakdown field with the presence of dielectric.
ΔE	Deviation from air breakdown field ($E_s - E_0$).
r_B	Value of r at which breakdown occurs.
d_w	Water transmission line plate separation.
R_L	Load resistance.
V_0	D.C. charging voltage.
V_s	Static breakdown voltage.
V_m	Holdoff voltage of multichannel spark gap.
ΔV	Voltage jitter.
i_m	Maximum current going into the load.
N	Number of conducting channels.
P	Multichannel switch pressure in PsiG.
t_r	Voltage risetime.
t_i	Current risetime.
τ	Breakdown time lag.
Δt	Jitter time.

CHAPTER 1

INTRODUCTION

1.1 Pulse Power Switch Requirements

During the last decade, there has been an increasing need for submegavolt, multichannel switches for electrical energy transfer in various pulse power applications, such as fast discharge laser systems. In order to achieve efficient operation and high output beam quality in multiatmosphere gas lasers, the production of volume glow discharges is necessary. ^{(1) (2) (3)} For this purpose, a transfer switch with low-inductance is required between the pulse forming network and the laser electrodes. In principle, inductance of the switch can be reduced to an acceptable level with intense multichanneling. It is known that the presence of a dielectric surface in the vicinity of a pair of spark gap electrodes usually enhances multichanneling (as will be shown later on), therefore a surface discharge switch seems to be appropriate.

Another desirable characteristic of the switch is a small jitter time. Since the laser gas must be preionized just before overvolting occurs, a precise knowledge of the switch closing time

is important for triggering the preionizer at the proper moment.⁽⁴⁾ The above requirement in general can be satisfied with high holdoff voltages. However, this usually means that a fast voltage charging rate is necessary and the performance of the switch is then limited by the fastest charging rate attainable. For this reason, an optimum design of the switch appears to be essential.

1.2 Multichannel Surface Spark Gap

Figure 1 illustrates a multichannel surface discharge spark gap (MSG) as developed by the National Research Council of Canada (NRC).⁽⁵⁾ One advantage of this switch is its simplicity of construction. The switch element is made of ordinary PC board with copper etched away to form the desired gap spacing. The entire unit is assembled with O-ring and high strength-insulating bolts for high pressure operation. The particular switch used in this experiment has a length of 66cm and a gap separation of 1.25 cm.

The basic factors involved in spark gap design are the internal geometry, the electrode and substrate material, the gas medium and its pressure, the voltage charging rate, the load characteristics, the repetition rate and the lifetime.⁽⁶⁾ An experimental switch was constructed in such a way that it allows

certain amount of adjustments in some of the above design parameters. The effects of these parameters on the performance of the switch can then be investigated using this device. A cross sectional view of the switch is shown in Figure 2. The perspex top piece of the switch is removable so that everything inside can be easily accessed from above. Different dielectric substrates and electrodes of various materials and shapes can then be put into the device. Gap spacing and electrode-substrate separation are also adjustable. Finally, the device can withstand a maximum gas pressure of at least 80 Psi so that the performance over a wide range of pressure can be tested.

1.3 General Outline of the Study

The main purpose of this study is to obtain a better understanding of multichannel surface switches so that the present design can be improved. The study is divided into three parts, namely, examination of the surface discharge phenomena, switch evaluation and lifetime testing, and modeling of the switch. In Chapter 2, a number of experiments which examines the physical processes involved in surface discharges under single channel static breakdown conditions is described. Different dielectric materials are examined to attempt to establish material dependences. The electrical performance of the NRC switch is investigated in

Chapter 3. The lifetime and the feasibility of extending it are studied using the experimental device. A brief description of the test assembly, monitoring system, and high-voltage measurement techniques is also included in the chapter. In Chapter 4, two models for the switch are presented. One of them is developed from an engineering point of view and the other one is based upon gas breakdown theory. Finally, observations and results from the above studies are summarized and conclusions are drawn in Chapter 5.

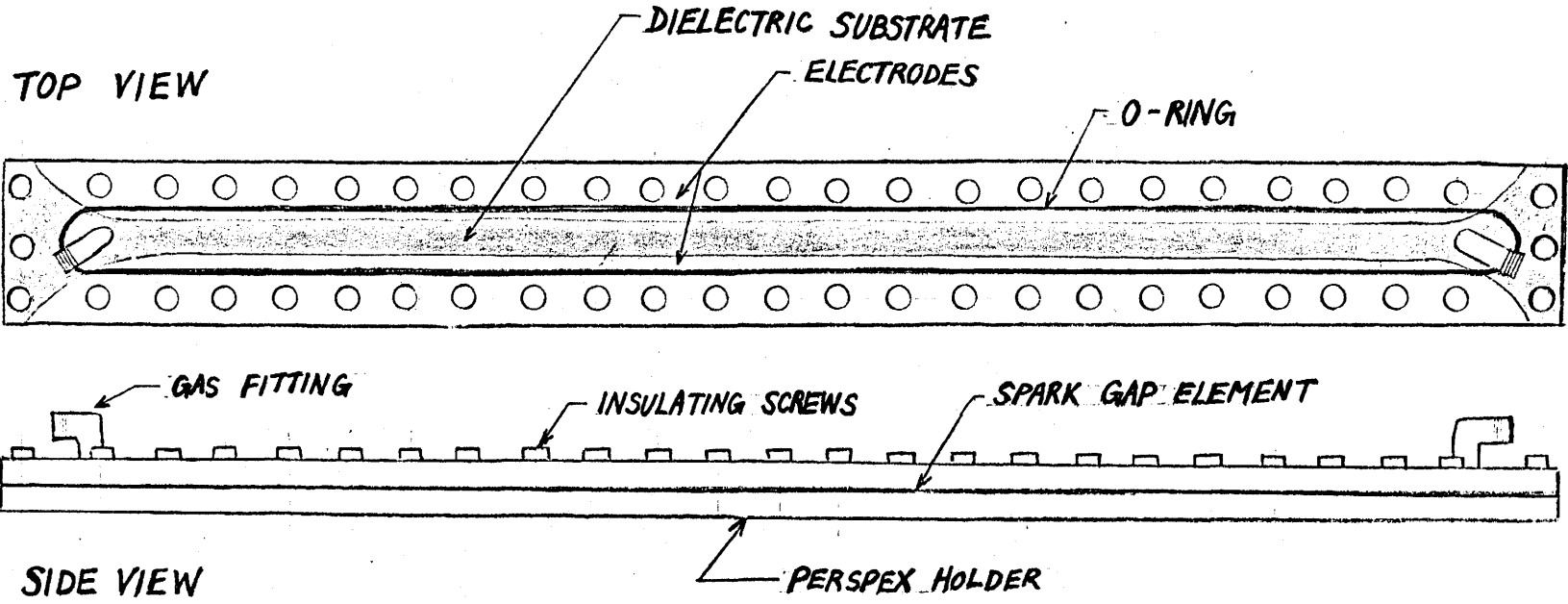


FIGURE 1

NRC Multichannel Surface Spark Gap Design

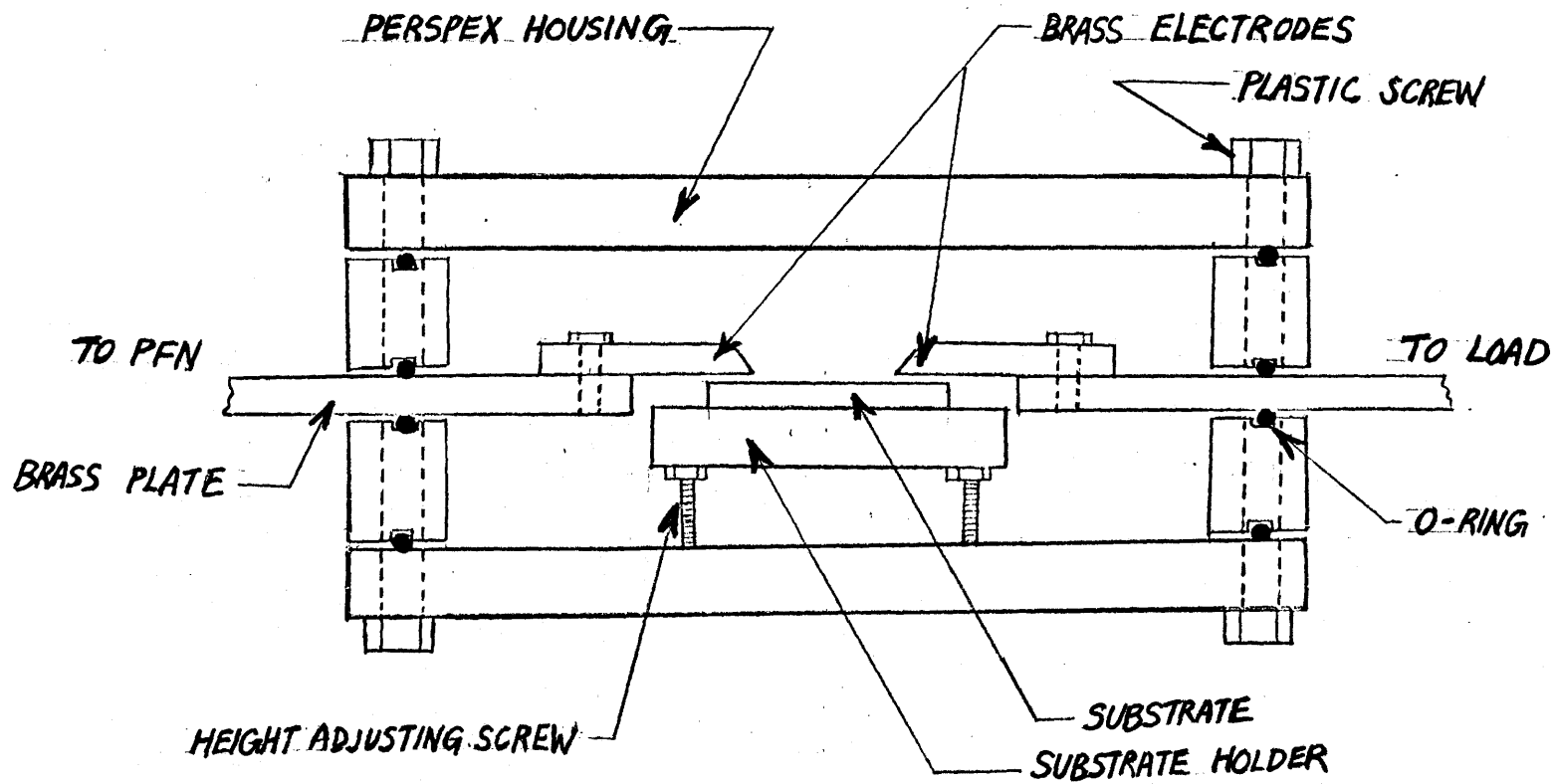


FIGURE 2

Cross-sectional View of Experimental Switch

CHAPTER 2

STATIC BREAKDOWN EXPERIMENTS

2.1 Physical Processes Involved in Surface Discharge

The physics of dielectric surface discharge phenomena is not well understood at the present. However, it is generally accepted that two essential conditions are required for a discharge channel to occur. They are (i) the supply of initial electrons and (ii) the formation of a high charge density conducting path between the two electrodes. For a self-breakdown gap, both conditions are strongly affected by the applied electric field strength and its configuration. The presence of a dielectric surface near the gap, which can possibly modify the field, would therefore be expected to have an effect on the discharge phenomena. A number of different processes may be involved at the same time in causing field distortion and these include the following: ⁽⁷⁾

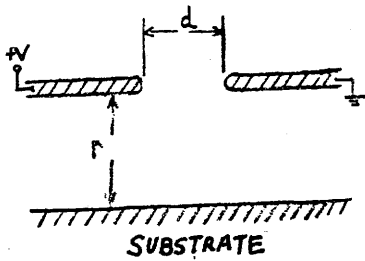
- (A) Geometry effect
- (B) Polarization effect
- (C) Surface conductivity effect
- (D) Surface trapped charge effect
- (E) Space charge effect

As an example of field distortion, the effect due to the presence of a metal strip is considered. The field configuration around a pair of single electrodes alone is shown in Figure 3(b). In Figures 3(c) and 3(d), the distorted fields caused by a positively biased metal strip with two different $\frac{d}{r}$ ratios are shown. It can be seen from the diagrams that the field intensity surrounding the cathode has been considerably enhanced and that distortion is more effective when the $\frac{d}{r}$ ratio is large. Figures 3(e) and 3(f) illustrate the cases with an unbiased metal strip. For a large enough $\frac{d}{r}$ ratio, it is observed that the field between the electrodes and the metal strip is much stronger than that between the electrodes themselves. All of the above diagrams are obtained by employing field sketching method. (8)

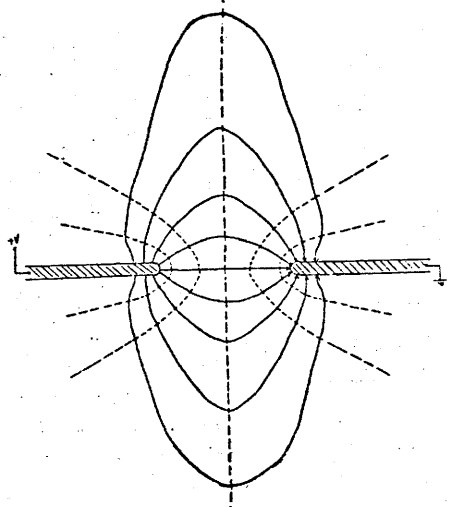
If a dielectric surface is present instead of a metal one, similar effect would be expected. However, the actual field configuration must be determined by the above mentioned processes. In the following section, the effect of each process will be investigated individually.

2.2 Experiments and Results

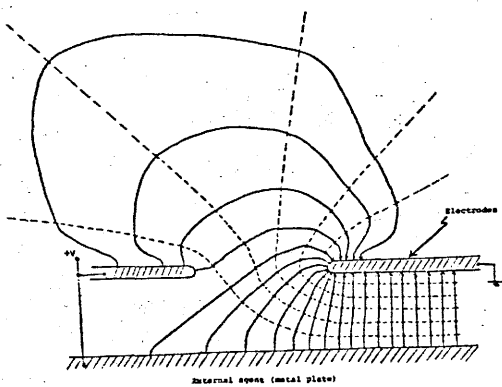
Several experiments were taken to study the different effects mentioned earlier. All of these experiments were carried



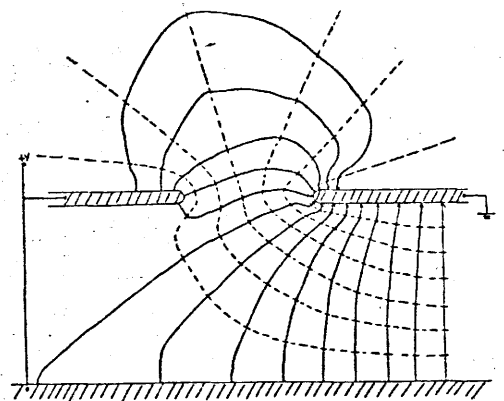
(a) NOTATIONS



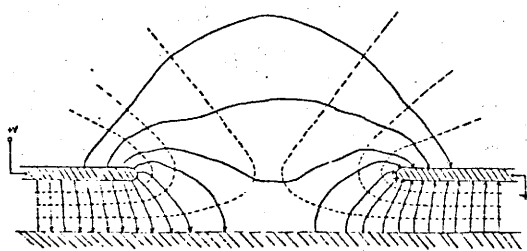
(b) ELECTRODES ALONE
 $\frac{d}{r} = 0$



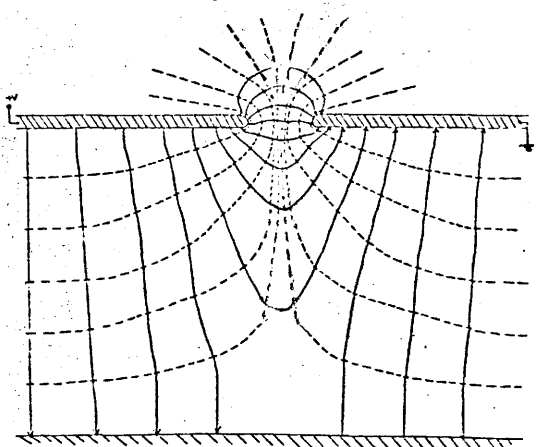
(c) WITH POSITIVE BIASED METAL PLATE, $\frac{d}{r} = 1.67$



(d) AS IN (c) BUT
 $\frac{d}{r} = 0.7$



(e) WITH UNBIASED METAL PLATE, $\frac{d}{r} = 5.0$



(f) AS IN (e) BUT
 $\frac{d}{r} = 0.2$

FIGURE 3

out under static self-breakdown condition with single spark channels. Hence neither the multichannel switch nor the pulse forming network was employed in this part of the study. Instead, a pair of copper electrodes with dimensions of $10 \times 1 \times 0.1$ cm and having one end rounded in shape was used to form the spark gap. The electrode separation, d , was set at 1.25 cm. All measurements were made at atmospheric pressure with a relative humidity between 50 to 59 percent. Uniform electric fields were also assumed in the calculations. The experiments are described as follows:

(A) Geometry effect:

This experiment was set up to study the distance dependence of the field distortion. The static breakdown voltage, V_s , was measured for different distances between the electrodes and the dielectric surface (r) and for different materials. Figure 4 shows the deviation from the air breakdown field caused by the presence of a dielectric (ΔE) as a function of r for teflon, quartz, and sintered oxide. It was observed that the static breakdown field dropped considerably when the dielectric surface was set at a small distance away from the electrodes. Other materials being examined showed similar behaviour and these include plastic, perspex, PPG glass, bakelite and copper. It was also observed that the maximum field deviation, which occurred

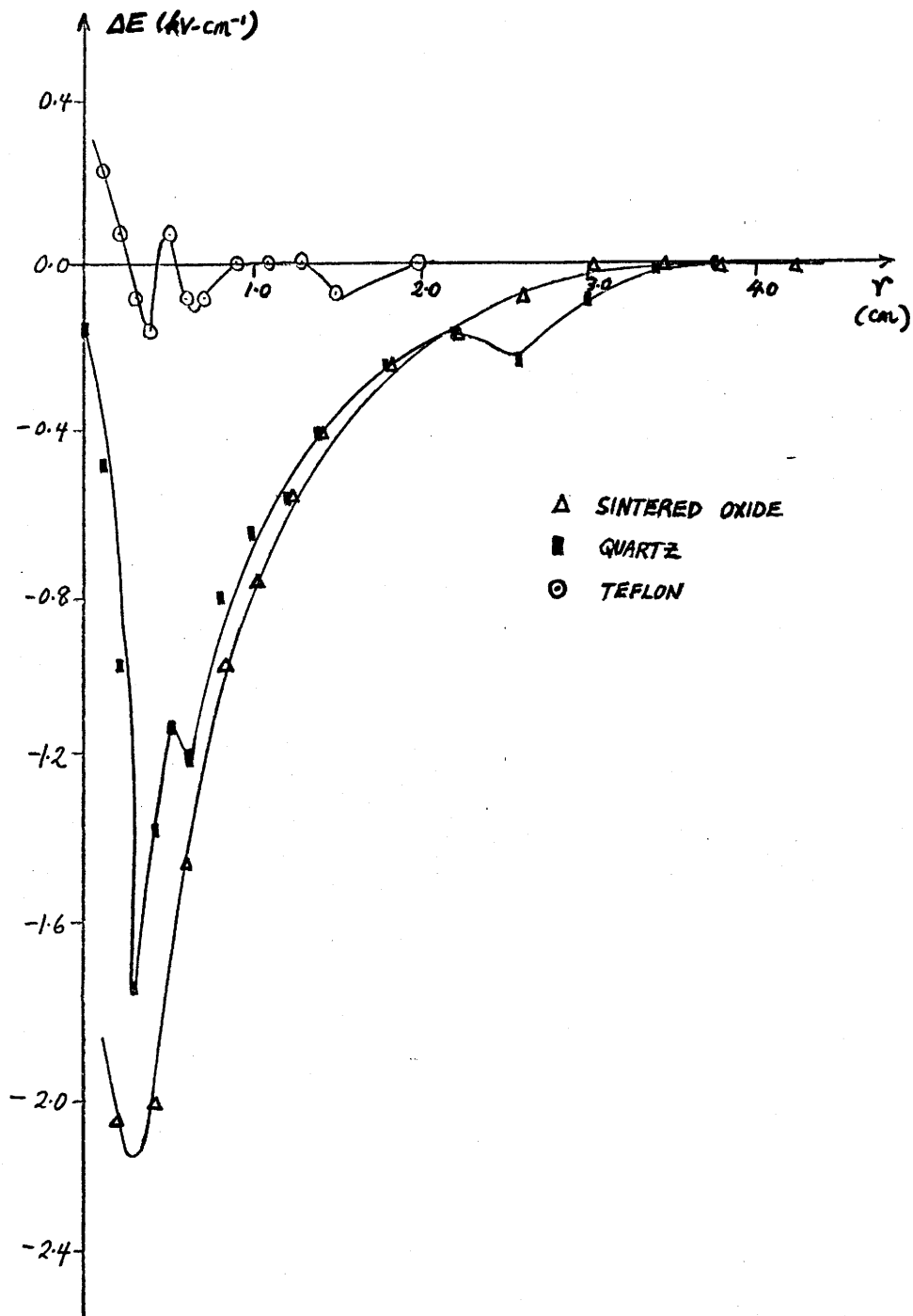


FIGURE 4

Deviation From Static Breakdown Field As a Function of r

at about $r = 3$ cm in all cases, seemed to be much more pronounced for materials with higher surface conductivity. Furthermore, less oscillations in distance dependence were observed for higher conductivity materials.

(B) Polarization effect:

The effect of dielectric polarization was studied in two different experiments. In the first one, the static breakdown voltage of the single electrode spark gap described earlier was measured with different dielectric materials in contact ($r = 0$ cm). The results are shown in Figure 5(a). In the second experiment, the gap voltage was set at a value that was slightly less than the static breakdown voltage in air. A dielectric material was put far away from the electrodes so that field distortion effect was not strong enough to cause breakdown to occur at that distance. Then the distance was decreased until breakdown has occurred and the value of r was recorded. This value is denoted as the breakdown separation, r_p . The procedures were repeated for different dielectrics. Results are shown in Figure 5(b). In both experiments, the measured data scattered considerably and no definite relationship was observed. However, it appears that the breakdown distance increases as the dielectric constant goes up.

(C) Surface conductivity effect:

The purpose of this experiment was to investigate the effect of surface conductivity on field distortion and hence on breakdown voltage. The experiment procedures were exactly the same as those in (B) except that the results were plotted against surface resistivity of the dielectrics. Again, Figures 6(a) and 6(b) show that the data are quite scattered and no significant conclusions may be drawn from them.

(D) Surface charge effect:

This experiment was set up to determine the influence of the applied field on the surface trapped charge density. The charge density was measured by a metal mesh collector and an electrometer. With a 400 V/cm field applied perpendicular to the dielectric surface, negative charges were sprayed on one surface until the charge density has reached a stable state. The field was then switched off and the surface charge density measured. The average change in charge density was found to be about 8%.

(E) Space charge effect:

In this experiment, the type of charges accumulated on a dielectric surface after it has been exposed to D.C. discharge was studied. The surface charge density was measured before

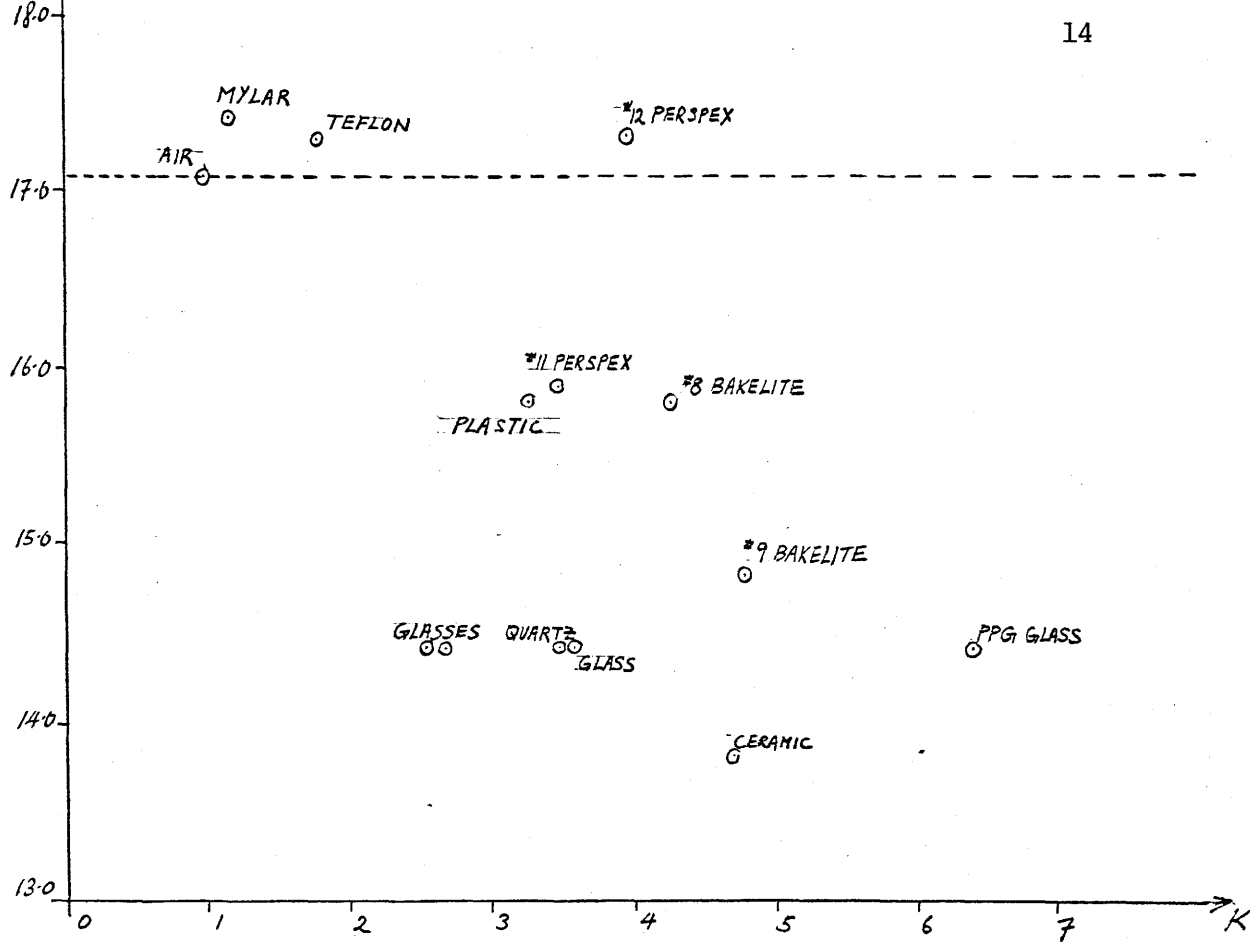


FIGURE 5(a) E_s as a Function of Dielectric Constant

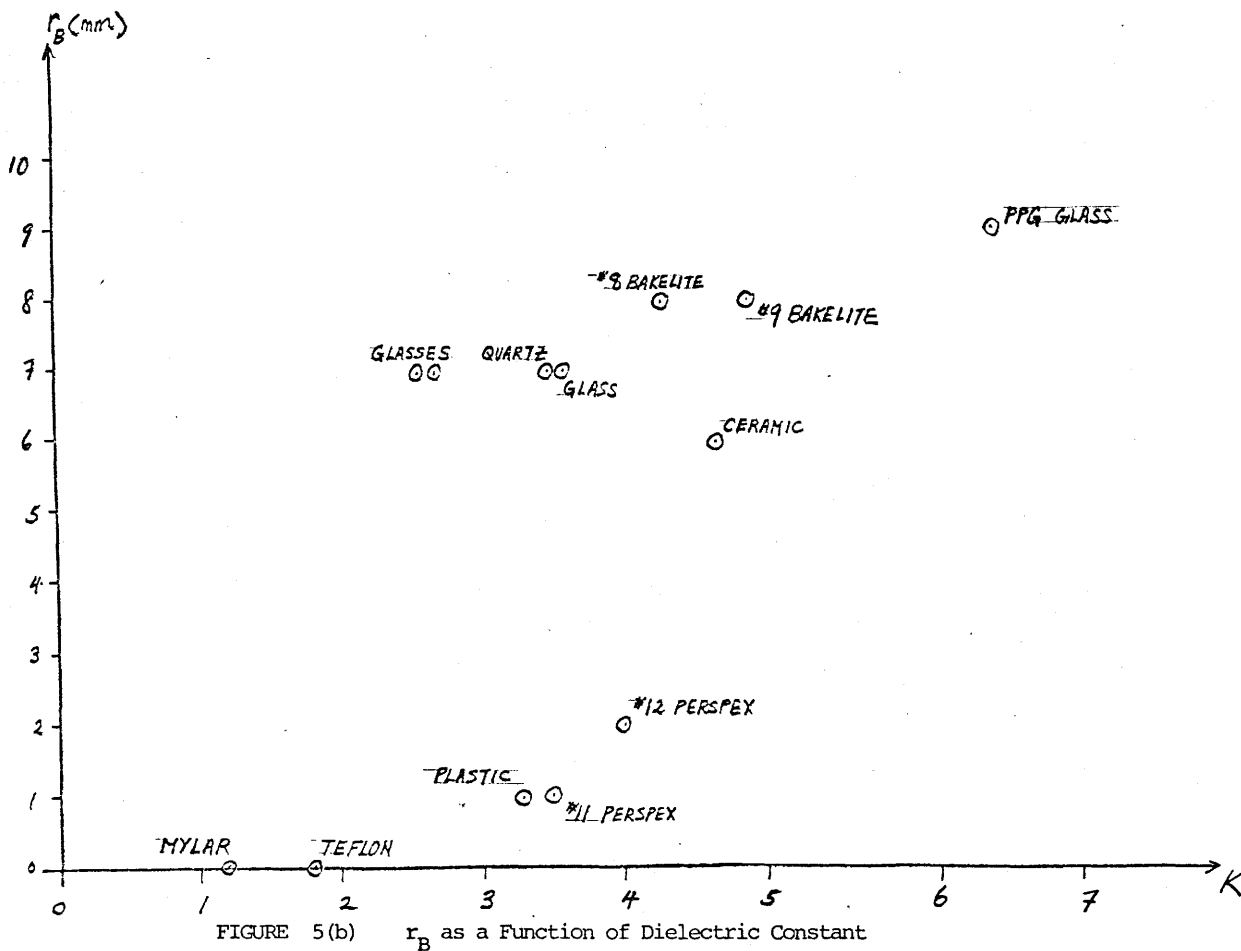


FIGURE 5(b) r_B as a Function of Dielectric Constant

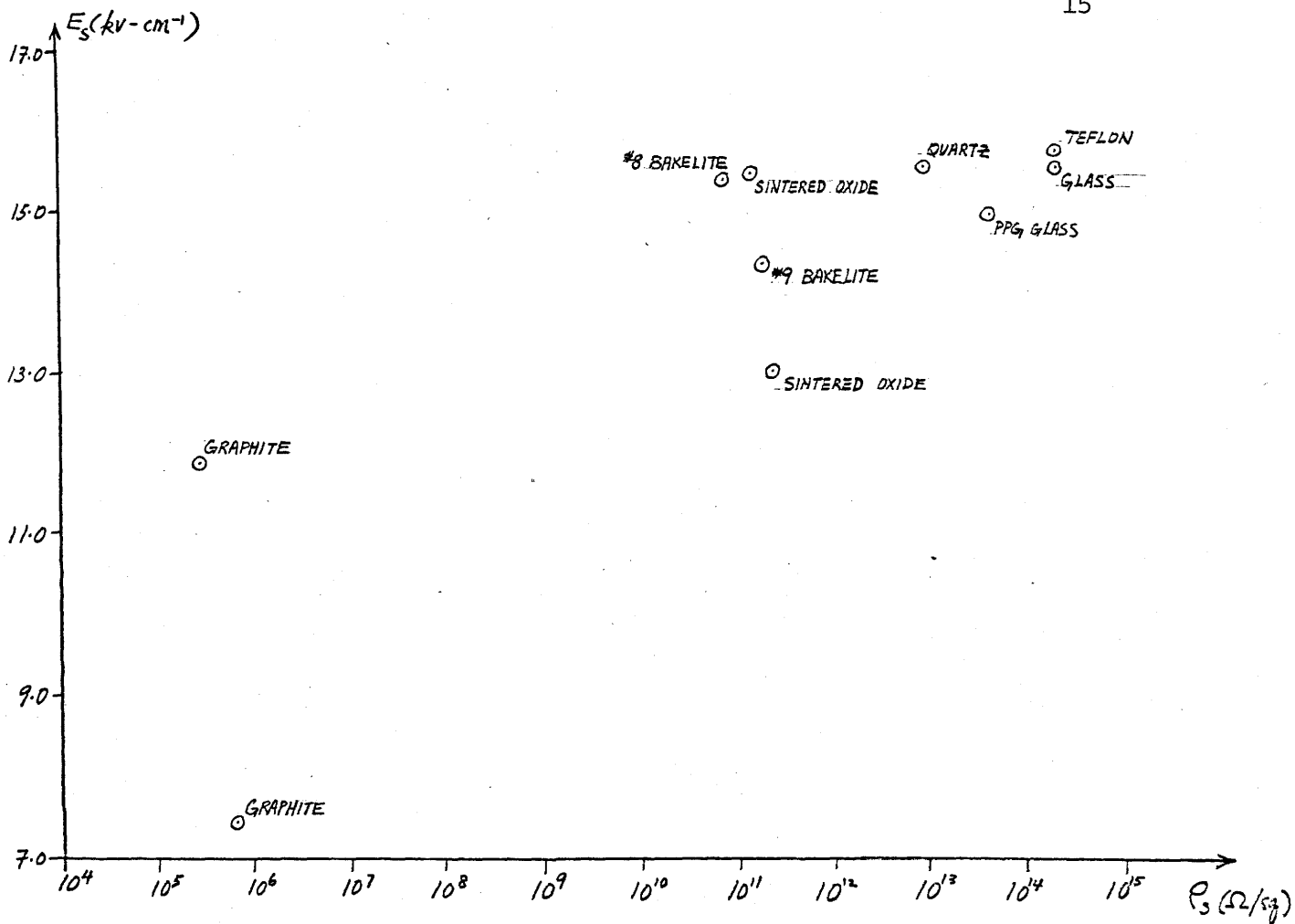


FIGURE 6(a) E_s as a Function of surface Resistivity

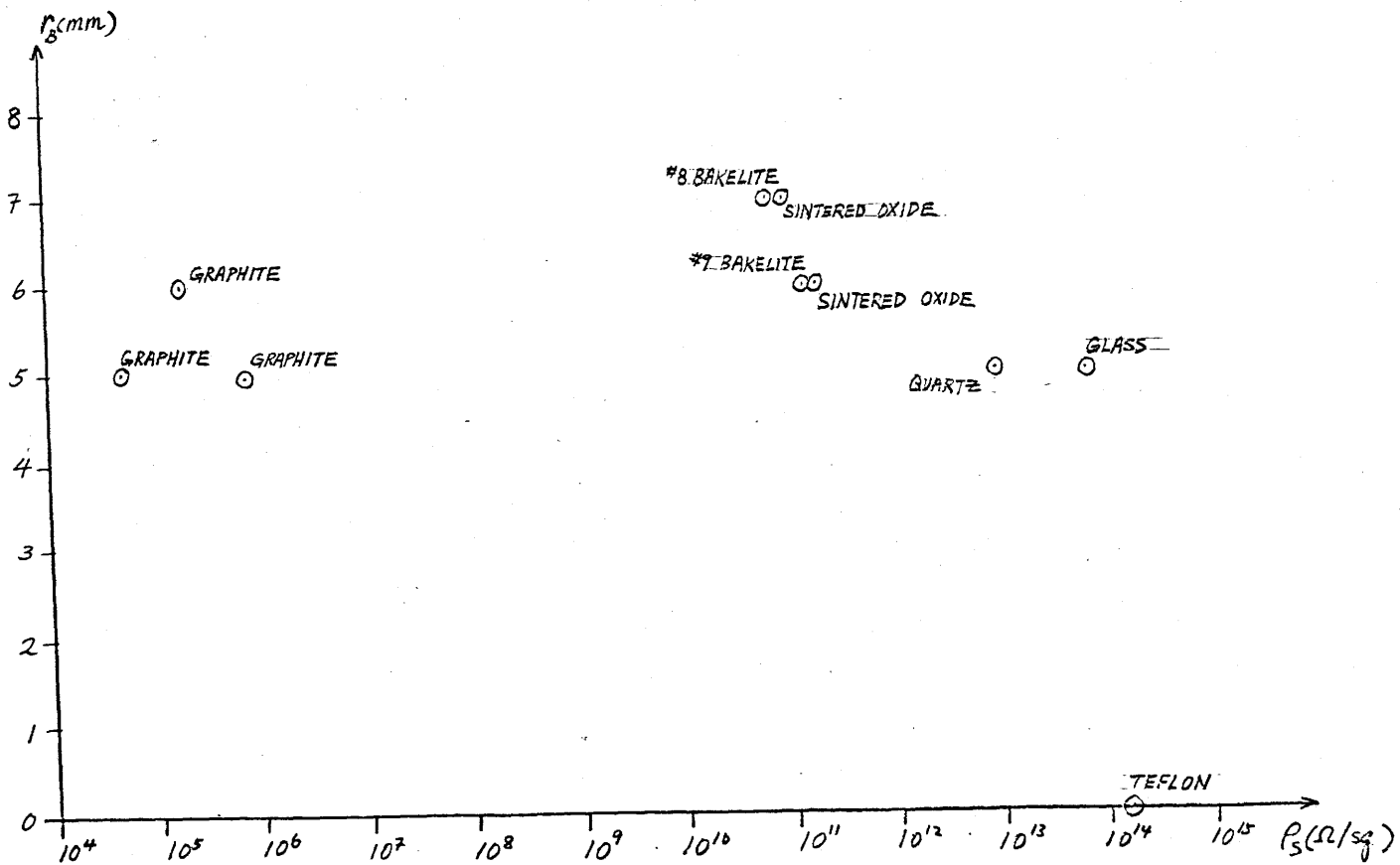


FIGURE 6(b) r_s as a Function of Surface Resistivity

and after the surface has been put at a distance of 2 mm away from a continuous D.C. spark for a period of one minute. The charges accumulated on the surface was found to be predominantly positive.

2.3 Discussion

The results obtained from the above experiments indicate that the underlying physics for surface discharges is extremely complicated even for the case of a single spark channel and under static self-breakdown situation. However, it appears that the field distortion plays the major role in the discharge phenomena. In general, the geometry effect, the polarization effect and the surface conductivity effect determine the charge distribution on the dielectric surface. The presence of additional charges such as surface trapped and space charges further complicates the field configuration. Each of the above processes contributes a part to the total effect. However, it is experimentally difficult to isolate individual effect from the others. This may explain the oscillatory results in Figure 4 and the scattered data in Figures 5 and 6. To illustrate this point more clearly, the following case is considered:

It has been shown that positive charges are accumulated

on the dielectric surface after it has been exposed to D.C. discharges. A dielectric with positive charges uniformly distributed on its surface would produce field distortion similar to that by a positively biased metal strip as shown in Figures 3(c) and 3(d). In either case, electric field surrounding the cathode is enhanced. For the case of a dielectric with high surface conductivity, redistribution of surface charges according to the external field may occur and the field configuration would therefore deviate from that in Figures 3(c) and 3(d). It is important to note that charge mobility is limited to the surface charges only, i.e., a dielectric is an insulator and no free electrons exist inside the bulk material. Instead, polarization of dielectric molecules occurs and the situation is somewhat similar to that of an unbiased metal plate as shown in Figures 3(e) and 3(f). Finally, as mentioned before, the degree of field distortion depends very much on the geometry or the $\frac{d}{r}$ ratio as illustrated in Figure 3. It is obvious that all of the above effects are involved at the same time and description of the electric field in terms of a single effect only is impossible.

The above discussion has indicated that independent study of each process involved in surface discharge is extremely difficult. The fact that some of the inconclusive nature of the experimental results may well be due to this reason.

Nevertheless, the combined effect on static breakdown field as a function of r as illustrated in Figure 4 is still a very useful piece of information. This will become clear when the surface discharge phenomena is studied under pulse charging condition as described in the next chapter.

CHAPTER 3

HIGH-VOLTAGE PULSE BREAKDOWN EXPERIMENTS

3.1 Resistive Load Test Assembly

The multichannel switch is inserted into the resistive load test assembly for the examination of its performance. A high-voltage D.C. power supply charges up the storage capacitor through a series of current limiting resistors up to a maximum voltage of 100 kV. When the capacitor voltage reaches the breakdown voltage of the single channel spark gap (SSG), the spark gap will fire and discharges the capacitor almost immediately. This process generates a high-voltage pulse with very fast risetime (about 100 ns in the present case) and therefore the above circuit is called the Pulse Forming Network (PFN). Nitrogen and SF₆ are the recommended gases to be used for the SSG. The self-breakdown voltage of the SSG is controlled by the gas pressure selected. Furthermore, the components of the PFN are usually immersed in transformer oil for high-voltage operation.

The generated pulse is then fed to the multichannel surface spark gap by means of a water transmission line. Same performance

has been reported for ceramic capacitor, oil, water and ethylene glycol transmission lines.⁽⁴⁾ In this study, water, which has a dielectric constant of 80, is utilized due to its capability of high-voltage operation and availability. Since the two parallel copper plates of the transmission line are only a few centimeters apart from each other, the use of deionized water is essential in preventing flashover to occur. It is also necessary to recycle the deionized water continuously as water resistance between the two copper plates can drop from about 2 k Ω to only 200 Ω within a few hours if recycling is not being done. The characteristic impedance of the water transmission line is found to be 1.35 Ω for a plate separation (d_w) of 2.5 cm and the corresponding transit time is calculated to be about 27 ns.

As the high-voltage pulse reaches the MSG, potential difference starts to build up across the spark gap electrodes until breakdown occurs. Then the voltage across the MSG collapses and energy is dumped into the resistive load rapidly. The load is made up of copper sulphate solution with two copper electrodes separated by a few centimeters apart. The advantages of using copper sulphate resistors are that they can absorb a large amount of energy quietly and safely, and that they have a resistive response into the several hundred megacycles region.⁽¹⁰⁾ The disadvantage is that it is very difficult to measure their resistances

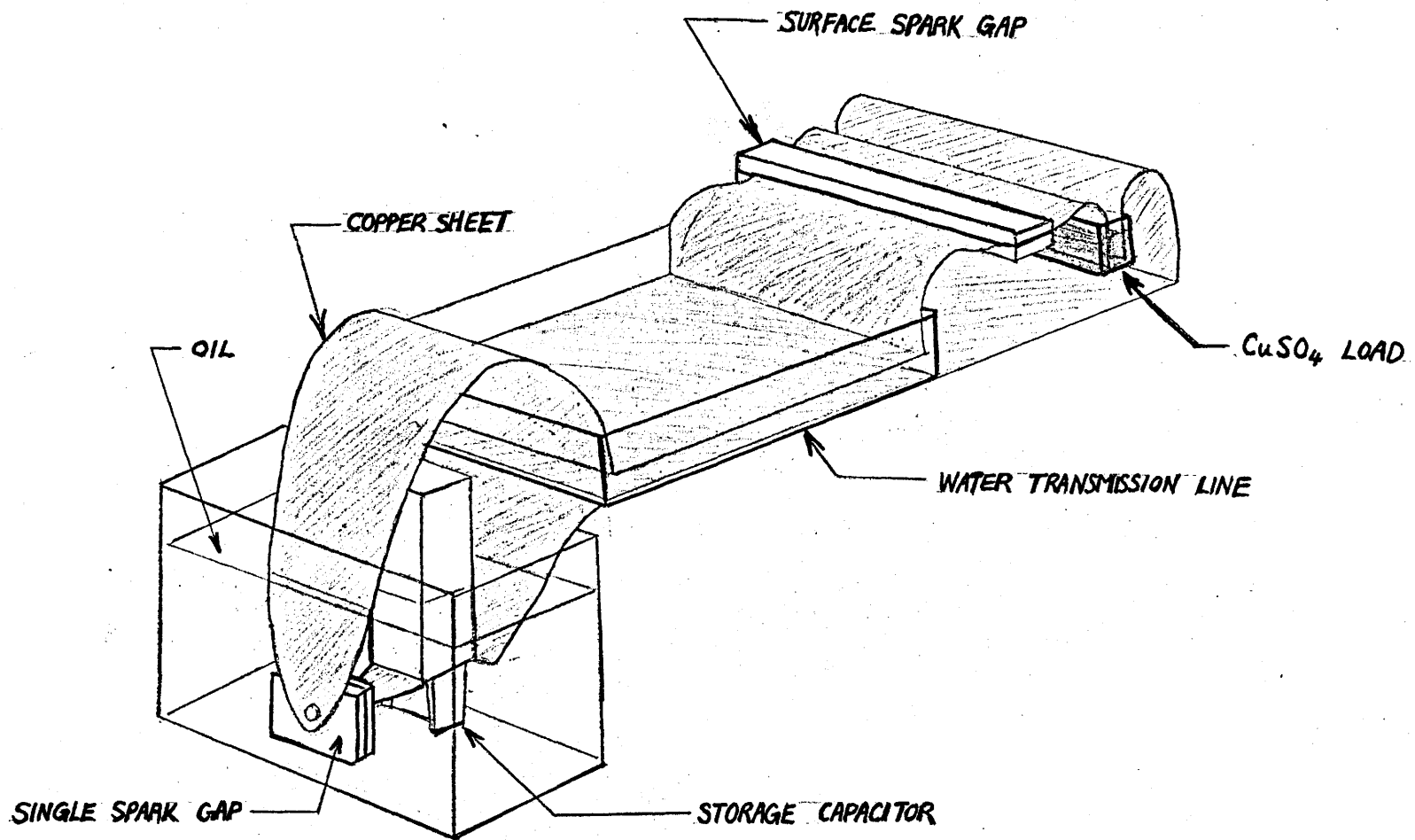


FIGURE 7

Schematic Representation of the Resistive Load Test Assembly

correctly because of the insulating films that formed on the electrodes.

3.2 Monitoring System

The two basic quantities that are of interest in an electrical circuit are, of course, voltage and current. In the present case, the voltage waveform measured at the output of the transmission line reveals information such as risetime of the charging pulse and the holdoff voltage of the MSG. Current is measured as the voltage drop across the resistive load and provides information about the energy delivery characteristic of the switch. In either case, the voltage waveform must be attenuated at least ten thousand times before it can be displayed on an ordinary oscilloscope. Once again, copper sulphate voltage divider is employed here for its advantages as explained before. This divider will attenuate the signal to a level that a high-voltage probe with peak voltage capability of 20 kV can be used. The probe, which has a resistive input impedance of about 3 k Ω , was claimed to have a risetime of less than 50 psec when it is matched into a 50 Ω load.⁽¹¹⁾ Further attenuation is obtained by using ordinary 10 x attenuators to bring the voltage within the range of the oscilloscope employed.

Besides the above electrical measurement system, there is also an optical measurement system involved. A fibre optic cable collects some of the light output of the surface spark channels and guides it down to a fast photodetector. The shape of the light pulse can then be displayed on the oscilloscope after it has been converted into an electrical signal. The risetime of the photodetector is less than 100 psec. Both the electrical (voltage) and optical (light output) signals can be displayed on the Tektronix 7834 scope at the same time and their phase relationship may be studied. Further details will be given in Section 3.4.

Finally, there is an electronic counter which would register the number of shots fired on the MSG. This information is important for the lifetime study of the switch. The counter operates by picking up the electromagnetic radiation generated from the sparks when the MSG fires.

3.3 High-Voltage Measurement Techniques

In high-voltage measurements, electromagnetic interference is usually a problem. Noise reaching the deflection system of the scope by different paths causes the display to be far different from the original waveform being measured. In general, distorted signals may be the result of one or more of the following modes

of noise generation: (12)

(A) Pick-ups through air:

Electromagnetic radiation generated by the system is usually picked up by cables and by the scope itself to cause a distorted waveform in high-voltage measurements. The problem can be avoided by putting the scope inside a Faraday cage and by moving the cage farther away from the radiating circuitry. All cables going into the scope should be shielded properly to reduce the noise.

(B) Power-line pick-ups:

Another way that the system generated noise can reach the scope is through its own power-line (< 30 MHz). This type of noise may be easily isolated when everything is perfectly shielded and when the scope input has been disconnected. The noise can be suppressed by conventional RFI (Radio-Frequency Interference) power-line filters. The filter is usually mounted on the outside of the Faraday cage so that the noise will be attenuated before entering the shielding cage.

(C) Pick-up loops:

Every effort should be made to make sure that the entire system is grounded at a single point and that the areas of any pick-up loops present are small if they cannot be eliminated.

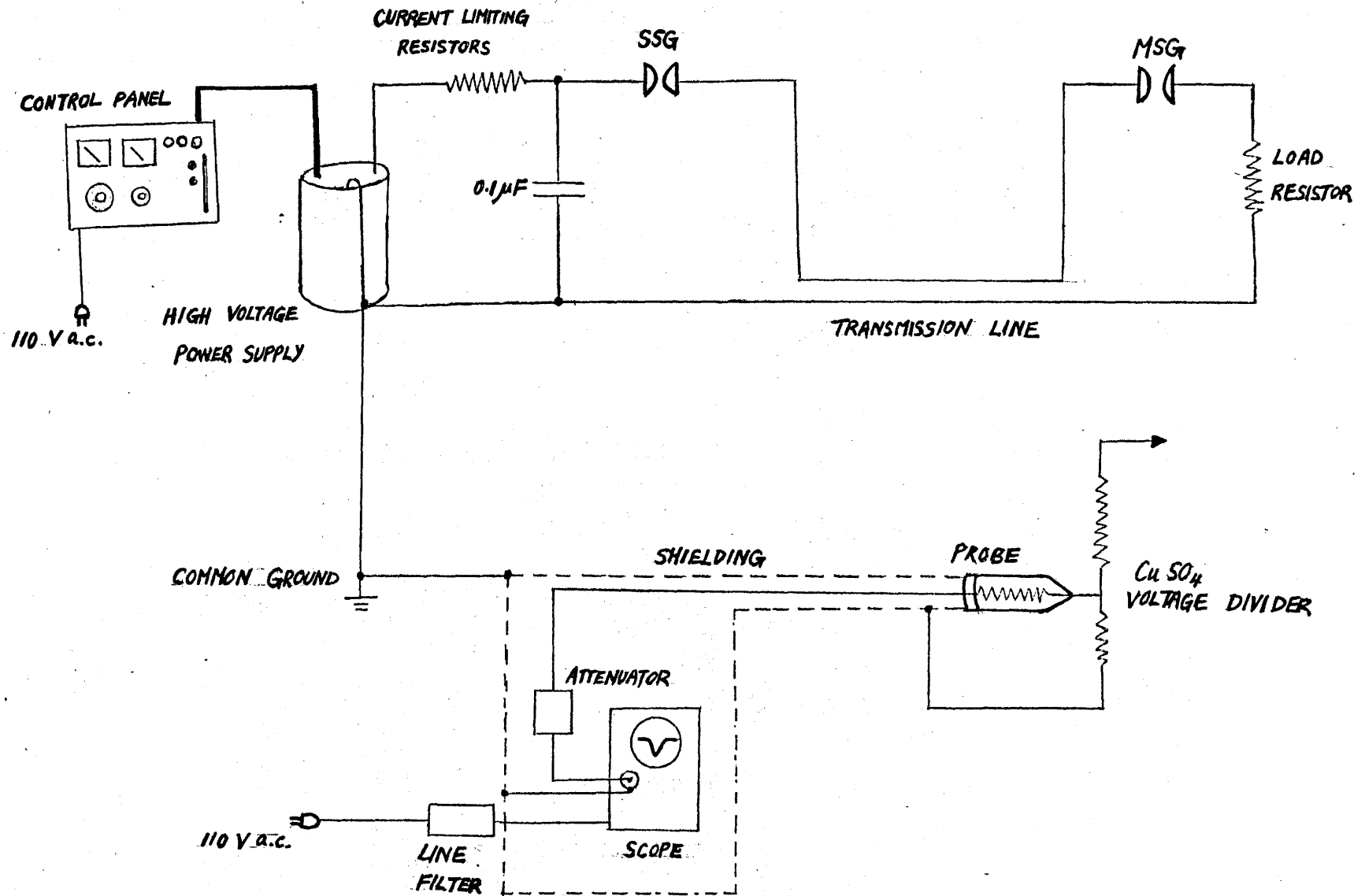


FIGURE 8

Complete System Layout Utilizing the ' tree wiring method '

Multiple grounding of the circuitry creates cable shield currents which will cause a voltage drop across the inner surface of the shield. This voltage drop is then superimposed upon the original signal inside the coaxial cable system and hence distorts the waveform. To eliminate this problem, all wires and cables should flow as if they are along the trunk and branches of a tree, and they should be tapped together closely. This type of arrangement is sometimes known as the 'tree wiring method'.⁽¹⁰⁾ Figure 8 illustrates how the method is employed in the present system.

3.4 Switch Performance

There are two time phases that are of importance in the evaluation of the multichannel switch. The first phase extends from the time when the SSG fires ($t = 0$) to the time the MSG starts to close ($t = t_r$). The second phase extends from t_r to the time when the current going into the load reaches its first maximum ($t = t_r + t_i$). The switch performance can be defined in terms of the holdoff characteristics in the first phase and the energy delivery characteristics in the second.

The quantities of interest in the holdoff region are the holdoff voltage V_m and the voltage risetime t_r . Holdoff voltage is defined as the maximum voltage that occur across the transmission

line output. It is desirable to have as high a holdoff voltage as possible so that a large amount of power can be transferred. At the same time, t_r should remain long enough so that the voltage charging rate can still be achieved. Both V_m and t_r were measured for the NRC switch under different conditions. The experimental results are given in Figures 9, 10 and 11. A transmission line plate separation of 2.5 cm and a load resistance of 3Ω were employed throughout the measurements.

The effects of the D.C. charging voltage V_0 on V_m and t_r are shown in Figures 9(a) and 9(b) respectively. It is observed that V_m stays more or less constant over a wide range of values of V_0 . On the other hand, t_r seems to decrease slowly with increasing applied voltage. Figure 10 shows the effect of P on V_m and it is observed that V_m increases rapidly with pressure at lower pressures and then remains more or less a constant for pressures exceeding about 30 PsiG. The effect of MSG pressure on t_r can be deduced from Figure 9(b) directly. In general, t_r is increasing with pressure for a certain value of V_0 . The above results have suggested that a high gas pressure is desirable for obtaining both a high holdoff voltage and a long risetime. The case can be illustrated more clearly by plotting t_r against V_m for different MSG pressures as shown in Figure 11, It has been reported previously that $V_m t_r^2$ is a constant for a given pressure of gas. (5) (9) Experiment results

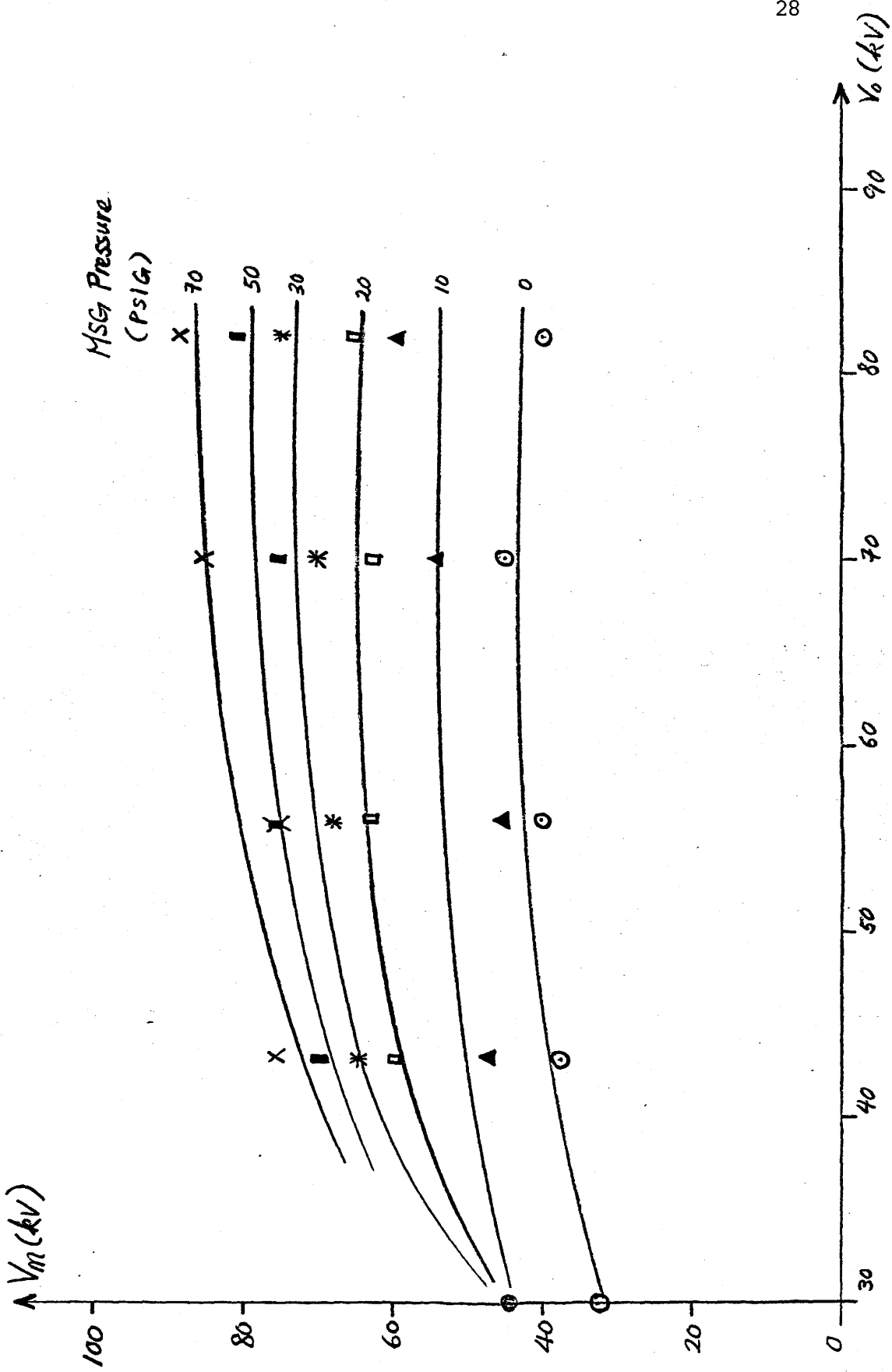
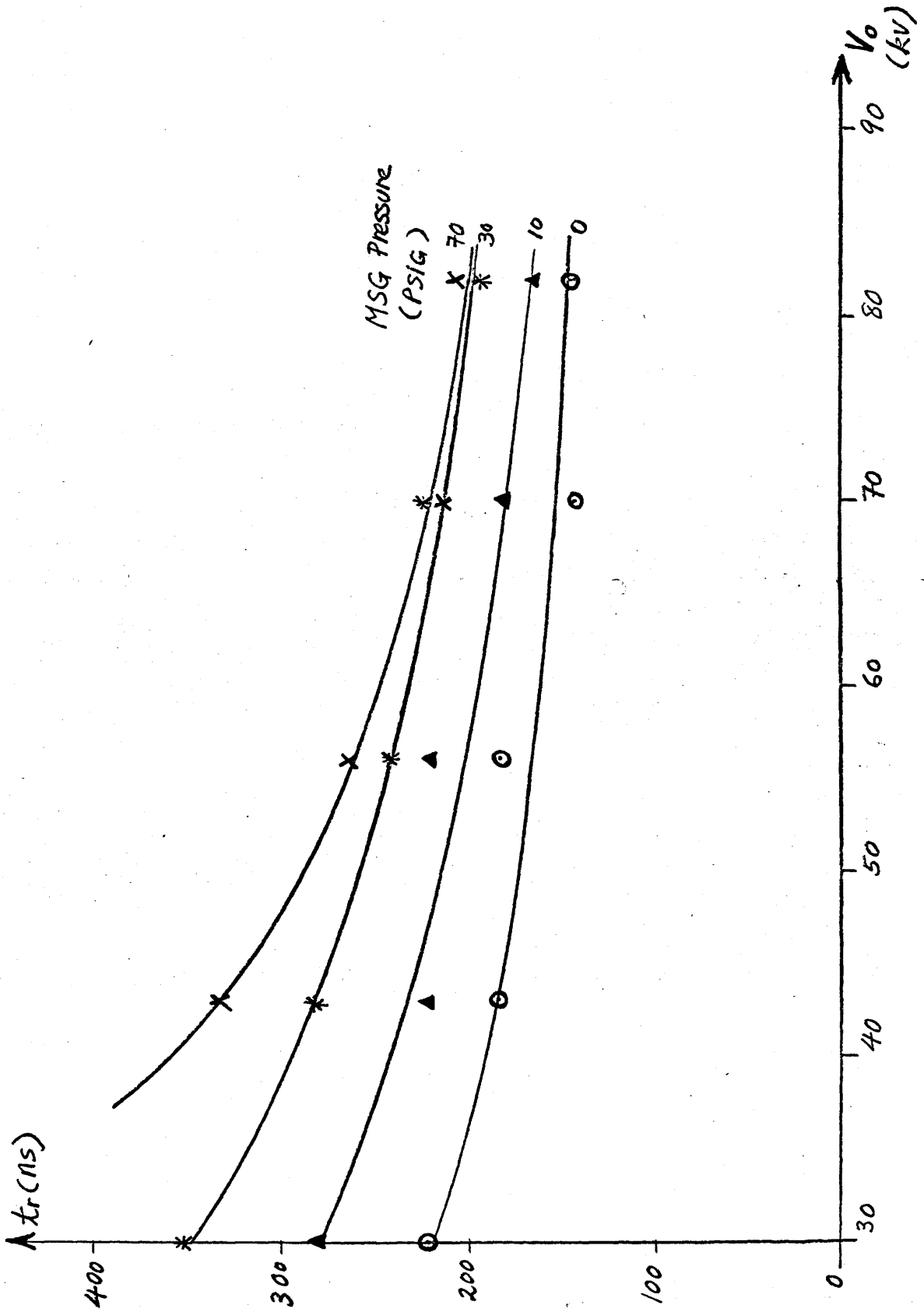


FIGURE 9 (a) Effect of V_0 on V_m For Different P's

FIGURE 9 (b) Effect of V_0 on t_r For Different P's

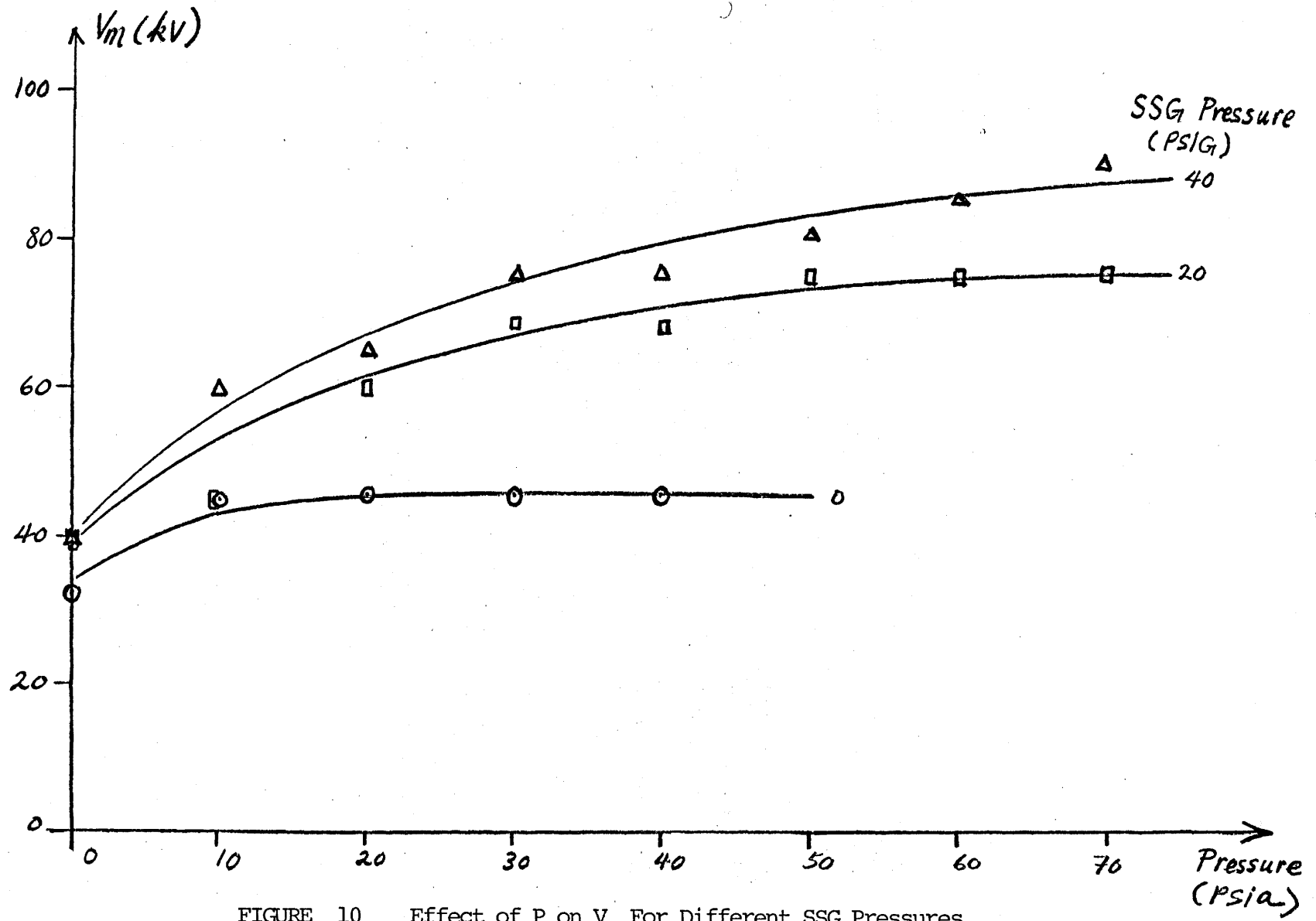


FIGURE 10 Effect of P on V_m For Different SSG Pressures

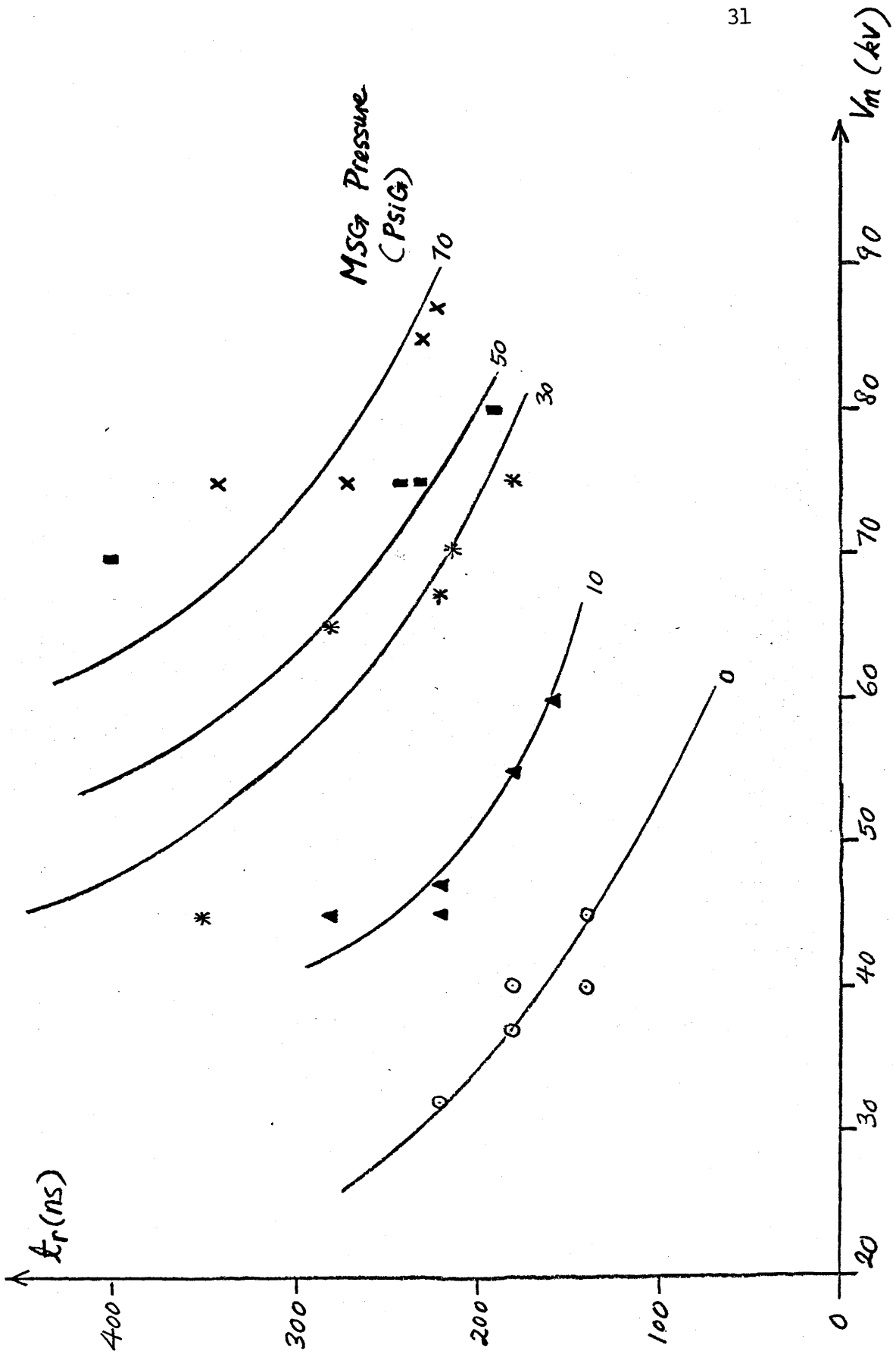


FIGURE 11 t_r Versus V_m

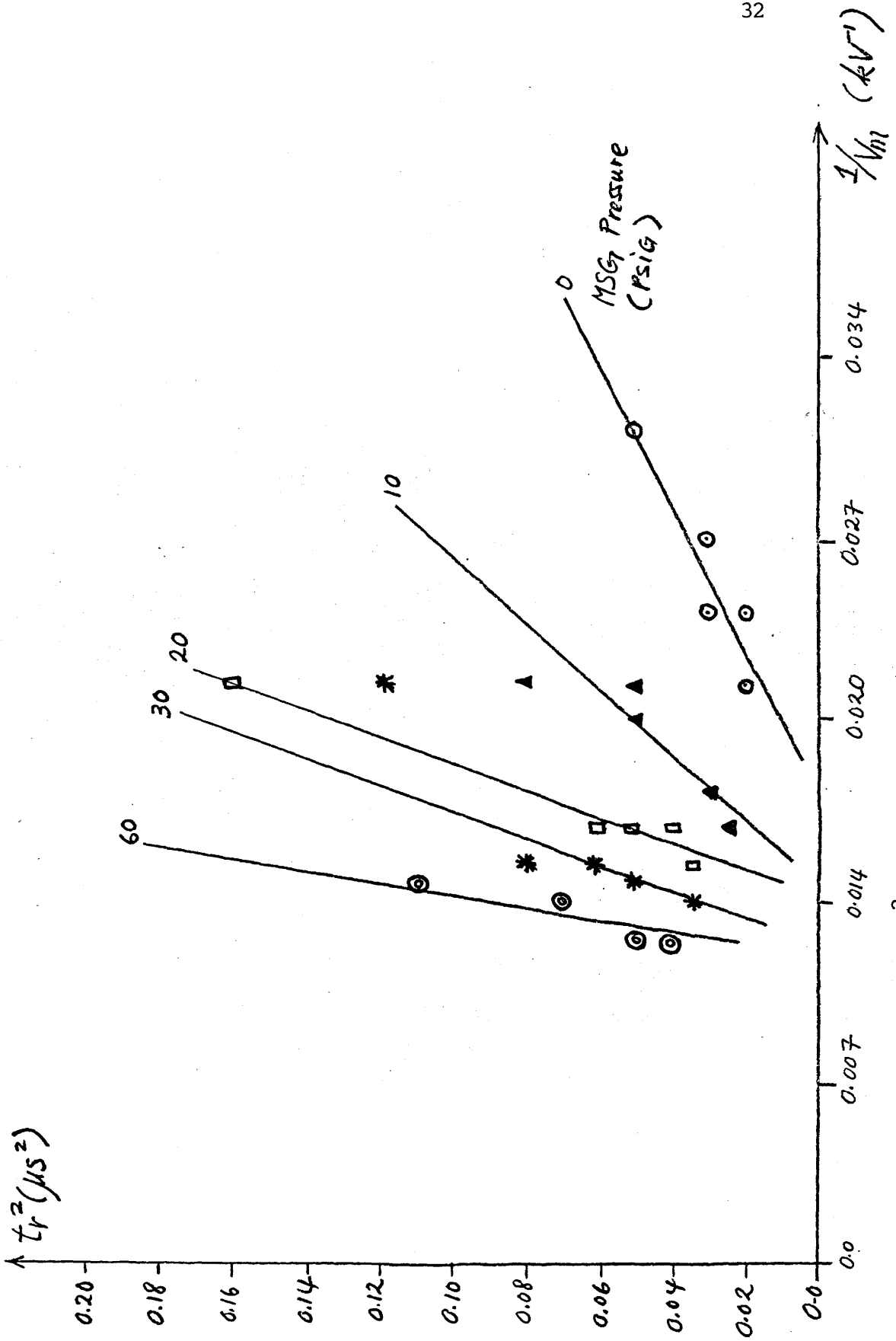


FIGURE 12 t_r^2 Versus I/V_m

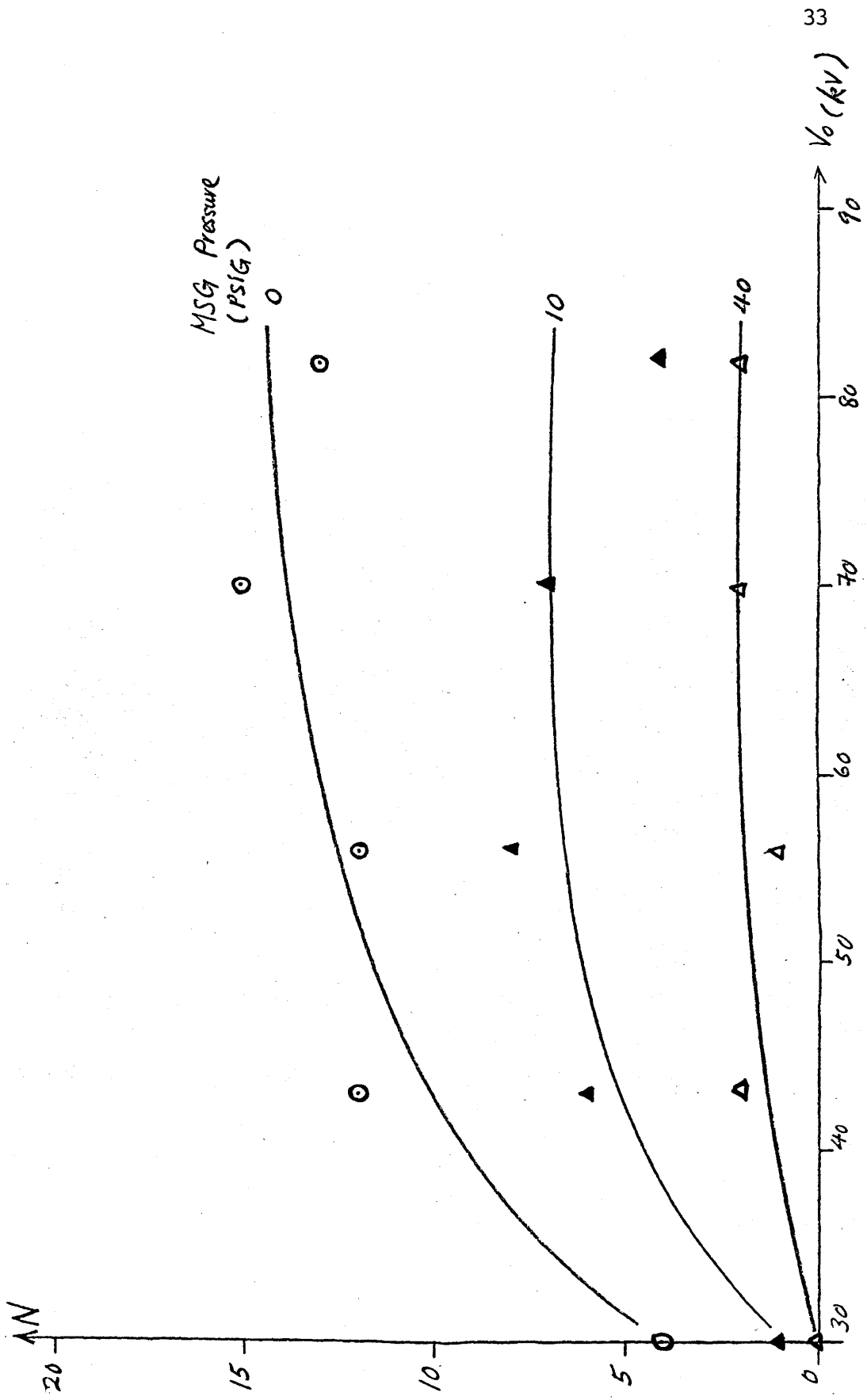


FIGURE 13 Effect of V_0 on N For Different Pressures

presented in Figure 12 seem to confirm that this is the case. The observed relationship appears to be in accordance with a physical model given in Section 4.2.

In the energy delivery time domain, the quantities to be measured are the number of channels N , the maximum current i_m and its risetime t_i , and the relative phases between $V(t)$ and $i(t)$. Figure 13 shows N as a function of V_0 for different MSG pressures. The experiment reveals that intense multichanneling can be achieved by increasing the D.C. charging voltage from 30 to 80 kV with proper adjustment of pressure. This is again in agreement with previous reports. ^{(5) (9)} As N decreases with P , a lower nitrogen pressure would be desirable for multichanneling. However, it has also been found earlier that a higher P is favourable for holdoff characteristics. In addition, while a large V_0 is essential for intense multichanneling, it also means that a smaller t_r is obtained. Hence a compromise must be made in order to achieve an optimum switch performance.

The phase relationship between $V(t)$ and $i(t)$ is illustrated in Figure 14(a). The measurements are obtained with the experimental switch used for life testing as will be discussed in detail in the next section. The substrate employed is quartz. Other experiment conditions are as follows:

$$d_w = 3.5 \text{ cm}$$

$$R_L = 1 \ \Omega$$

$$P = 15 \text{ PsiG}$$

$$V_0 = -50 \text{ kV}$$

From Figure 14(a), it can be seen that current starts rising when the voltage begins to collapse. The voltage and the current are therefore exactly 90 degrees out of phase at the moment when breakdown occurs. One can consider the phase difference as being caused by an inductive element in the circuit. In fact, the MSG can be think of as a resistor and an inductor in series. Before breakdown occurs, the resistance is infinite and the inductance assumes some arbitrary value. When breakdown occurs, the resistance drops rapidly down to a few ohms and current starts flowing. Both the resistance and the inductance are functions of time and decrease as the conducting channels expand to become larger in cross section. Figure 14(b) shows the calculated impedance as a function of time.⁽¹³⁾ It is observed that the discharge impedance drops from infinity down to about 10 ohms in less than 40 ns. The resistance and the inductance time functions, however, cannot be separated from each other using the above information. Nevertheless, discharge impedance does provide a way of characterizing the switch and hence allows meaningful comparison of performance measurements.

The light output of the spark channels are collected by an

optical fibre and after being converted into an electrical signal by a fast photodetector, the waveform can be displayed on the scope. A typical light pulse is shown in Figure 15. Since the acceptance angle of the fibre is small, only light emitting from a certain length of the spark gap will be collected. Therefore the amplitude of the displayed pulse depends very much on the location of the spark channels and carries little significant information. The duration of the light pulse should correspond to the time period in which the switch is closed. Figure 15 suggests that the spark gap remained closing for approximately 4 μ s. In addition, the waveform of the light pulse may also describe the electrical energy transfer time function since light itself is a form of energy. Finally, a scope picture showing the phase relationship for voltage, current, and light is given in Figure 16. Both current and light start to appear just after the voltage has reached a maximum as expected.

3.5 Life Testing

Another factor that must be taken into consideration in the switch design is the lifetime of the device. An experimental switch described earlier is used to study this aspect. Each of the substrate samples is inserted into the experimental switch and examined before and after the switch has been operated for 10,000 shots under the following conditions:

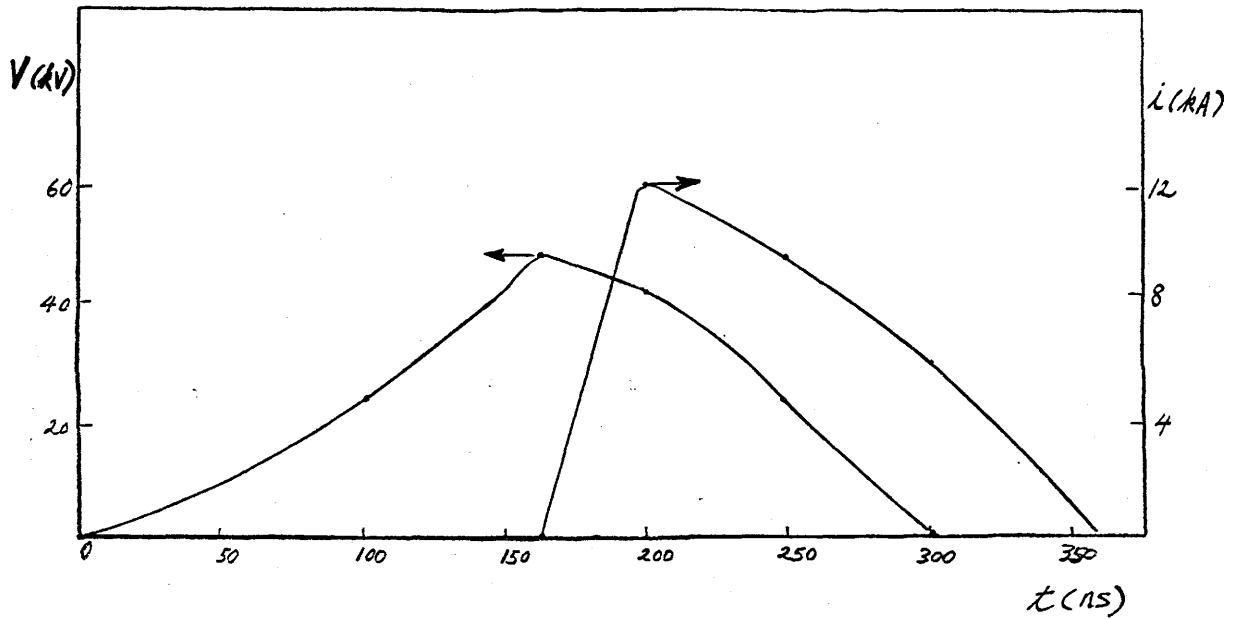


FIGURE 14(a) Voltage and Current as a Function of Time

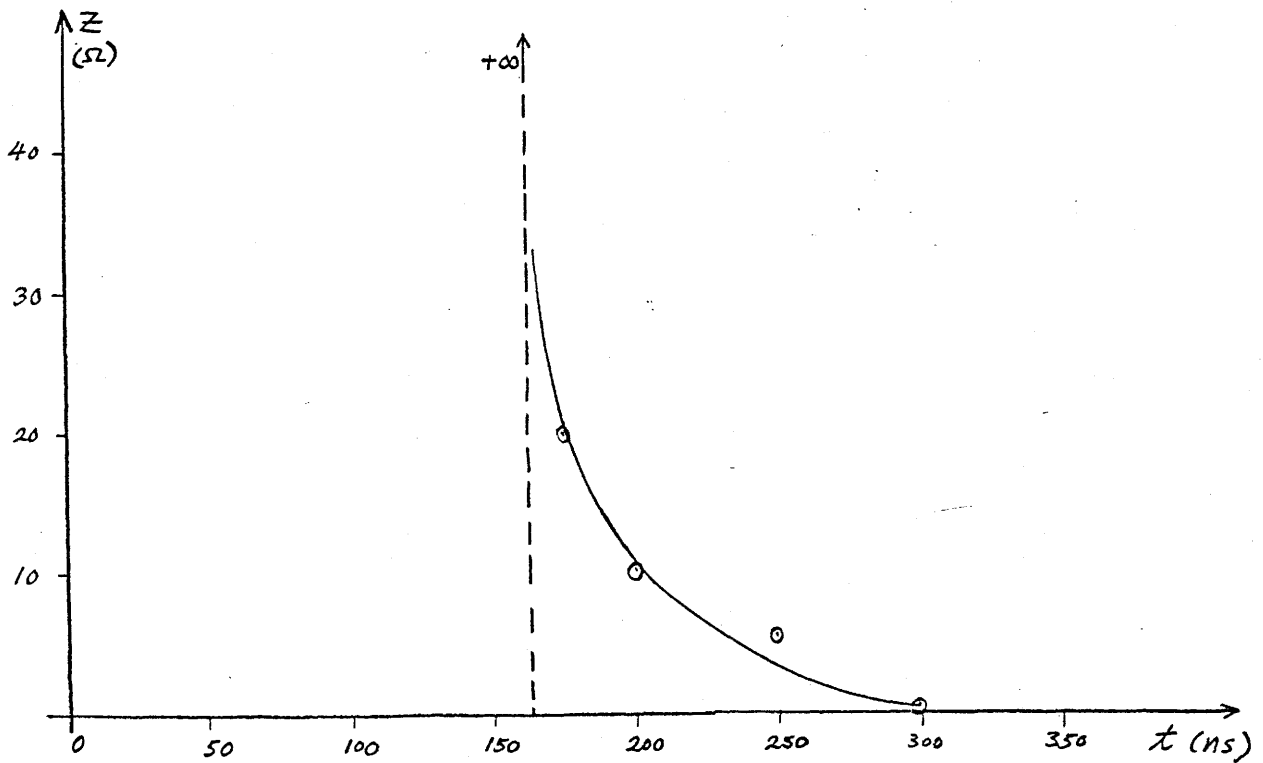


FIGURE 14(b) Impedance as a Function of Time

$$V_0 = -62 \text{ kV}$$

$$d_w = 3.5 \text{ cm}$$

$$P = 15 \text{ PsiG}$$

$$R_L = 1 \Omega$$

The total energy switched during each test is calculated to be $2 \times 10^6 \text{ J}$.

Lifetime of the substrates is studied in terms of the surface erosion and the degradation in performance. The surface erosion seems to have been caused by melting and evaporating as well as ion sputtering.⁽¹⁴⁾ The amount of material being removed per 100 kJ for each substrate is given in Table 1. It appears that quartz suffers the least amount of surface damage among the samples. This is not too surprising as the melting point of quartz is comparatively higher than the other materials studied. In contrary to the substrate erosion, the electrode erosion seems to be acceptable. Only 0.1 mm^3 of brass material is removed per 100 kJ switched. For the studying of performance degradation, the holdoff voltage, the static breakdown voltage (at one atm of nitrogen), and the number of discharge channels are all measured before and after the 10,000 shots. In general, both V_m and V_s drop only slightly while N decreases significantly after each test. For PC board and sintered oxide samples, resistive coatings are formed on the substrate surface and V_s cannot be measured (i.e. the substrates behave like linear

resistors and breakdown does not occur). Quartz is once again found to be the best among the samples (see Table 1).

From the above results, an insulating material with evaporation and sputtering rate of at least one order of magnitude lower than that of quartz seems to be required for an acceptable lifetime of, say, 10^7 shots. Another alternative would be to separate the substrate from the electrodes by some distance so that direct contact of the surface with the plasma channels may be avoided. However, it has been shown in the previous chapter that the static breakdown voltage is considerably reduced when the substrate is placed at a small distance from the electrodes. In order to observe what the effect might be on multichannel operation in the pulse breakdown case, an experiment is carried out with PC board to measure N for various substrate-electrode separations. The results are shown in Figure 17. It is seen that the number of channels decreases from 15 to about 4 when the substrate is moved from 0 to 5 mm away from the electrodes. This observation explains why less channels are obtained after surface erosion has taken place in the lifetime experiments. In addition, since the number of channels remained at 4 after the PC board is completely removed, it is concluded that the substrate has practically no effect on multichanneling when it is placed at more than 5 mm away from the electrodes. It is also interesting to point out that different dielectric samples were

shown to be able to induce static breakdown when placed at a distance varying from 0 to 10 mm away from the electrodes (see Figures 5(b) and 6(b)).

The above observations suggest that a small substrate-electrode separation may be used to minimize substrate damage without considerably affecting the switch performance. An experiment is carried out to look into the feasibility of this arrangement. Sintered oxide substrate is kept at 2 mm below the electrodes and 10,000 shots are accumulated under the same conditions as before. Little difference in performance from the previous sintered oxide experiment is found. However, the degree of substrate surface damage is observed to be much less for the present case. This suggests that the idea may indeed be used to extend the lifetime of the switch.

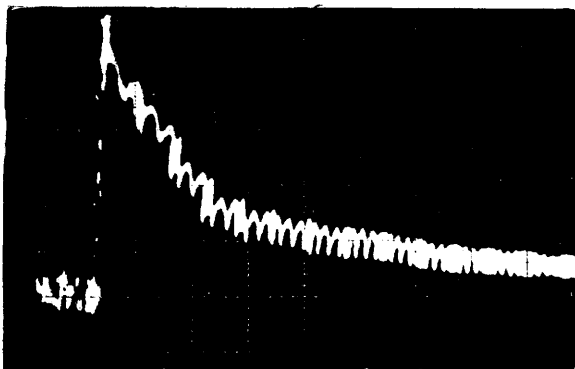


FIGURE 15
 A Typical Light Pulse
 Hor.: $0.5\mu\text{s}/\text{div}$
 Vert.: $50\text{mV}/\text{div}$

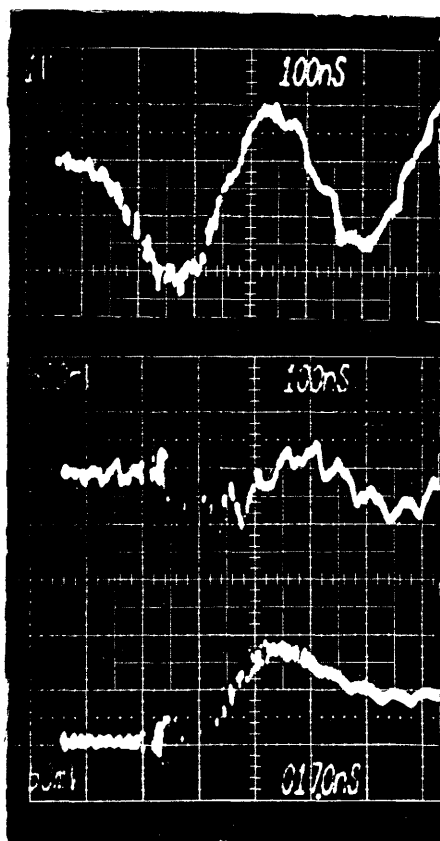


FIGURE 16

(a) Voltage Waveform

(b) Current Waveform

(c) Light Pulse Waveform

SUBSTRATE	V_m (KV)		V_s (KV)		N		Material Removed $\text{mm}^3/100\text{KJ}$
	Initial	Final	Initial	Final	Initial	Final	
PC Board	68.0	62.0	20	10M Ω	15	4	22.0
Bare Ceramic	65.3	63.0	22	20	10	6	5.0
Sintered Oxide	76.8	69.1	18	22M Ω	8	5	7.0
Quartz	61.4	58.8	18	17	10	9	4.0
Teflon	56.0	56.0	19	18	12	8	30.0
Brass Anode	-	-	-	-	-	-	0.1

TABLE 1 Life testing results of various substrates and brass electrodes. Initial readings were taken after ten shots of approximately 200J pulses while final readings were taken after 10,000 shots. Total energy switched during test was 2.10^6J .

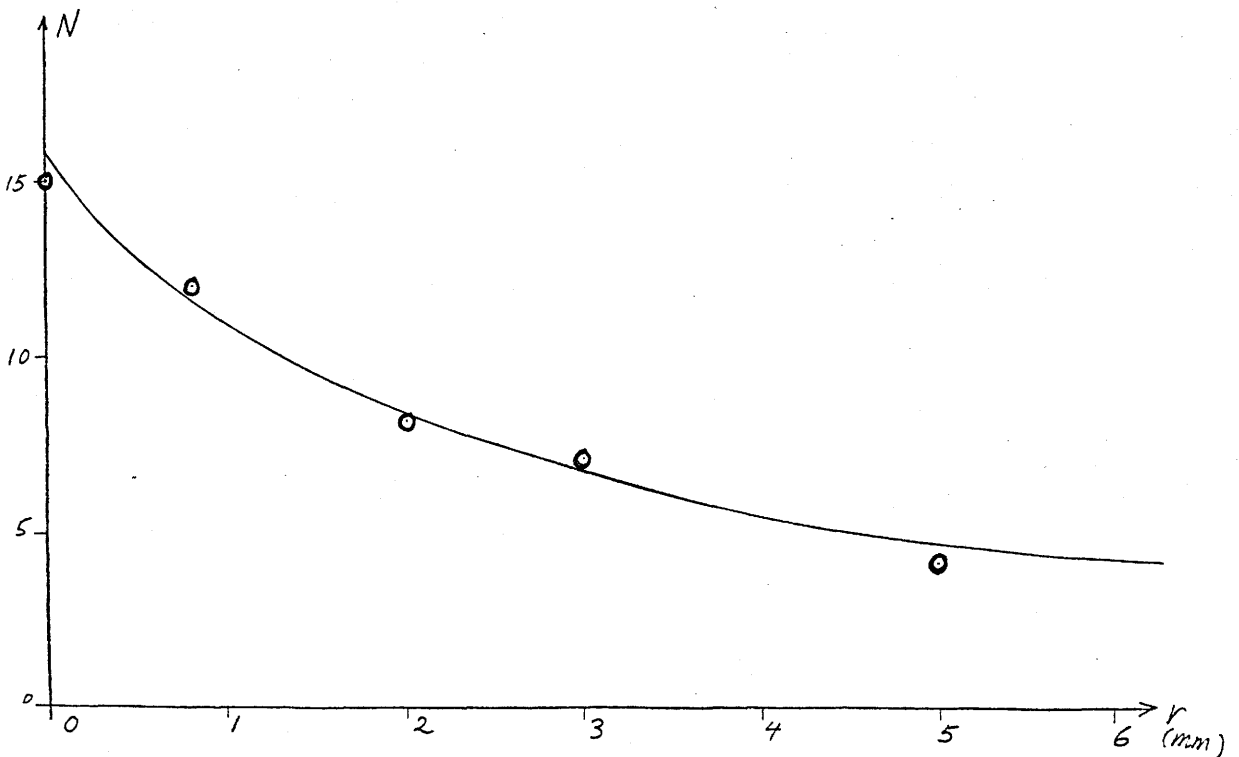


FIGURE 17 N Versus r

CHAPTER 4

MODELING OF MULTICHANNEL SWITCH

4.1 Engineering Model

The modeling of the switch will be done in two different ways. The first model follows the electrical engineering approach. The switch is being treated as a black box and is assumed to be replaceable by ideal circuit components. With all other external circuit parameters defined, network analysis can be used to determine voltages and currents at various points of the circuit. The second model attempts to cover the underlying physics involved and is to be discussed in the next section. Only the engineering model will be dealt with at this moment.

Figure 18(a) gives the equivalent circuit for the resistive load test assembly.⁽¹⁵⁾ The water transmission line is replaced by a capacitor C_2 . This is justified by the fact that the transit time of 27 ns is shorter than the pulse charging time of at least 100 ns. As discussed before, the MSG can be considered as an inductor (L_2) and a resistor (R_2) in series.⁽¹⁶⁾ In general, the inductance and the resistance vary with time as the plasma channel expands and

changes in diameter. Both quantities decrease rapidly after S_2 closes ($t = t_0$) as expected. It is assumed that R_2 jumps from infinity to 0.4 ohm at $t = t_0$ and then increases slowly back to infinity. The exact forms for $R_2(t)$ and $L_2(t)$ cannot be determined directly. For calculation purpose, the following forms are assumed (see also Figure 18):

$$R_2(t) = R_0 \exp\left(\frac{t - t_0}{\tau_R}\right) \quad (1)$$

$$L_2(t) = L_0 \exp\left(-\frac{t - t_0}{\tau_L}\right) \quad (2)$$

In this study, $R_2(t)$ is assumed to be the same in every case and the effects of varying L_0 and τ_R are examined. By defining

$$L_p = L_L + L_2(t) \quad \text{and}$$

$$R_p = R_L + R_2(t) \quad ,$$

one can write down immediately for the circuit,

$$L_1 \frac{di_1}{dt} + R_1 i_1 + \frac{q_1}{C_1} + \frac{q_2}{C_2} = 0 \quad (3)$$

$$L_p \frac{di_3}{dt} + R_p i_3 - \frac{q_2}{C_2} = 0 \quad (4)$$

$$i_1 - i_2 - i_3 = 0 \quad (5)$$

The above equations can be rearranged to obtain a set of first order differential equations:

$$\frac{di_1}{dt} = -\frac{1}{L_1} \left(R_1 i_1 + \frac{q_1}{C_1} + \frac{q_2}{C_2} \right) \quad (6)$$

$$\frac{di_2}{dt} = -\left(\frac{1}{L_1 L_p}\right) \left\{ (L_p R_1 - L_1 R_p) i_1 + L_1 R_p i_2 + \left(\frac{L_p}{C_1}\right) q_1 + \left(\frac{L_p + L_1}{C_2}\right) q_2 \right\} \quad (7)$$

$$\frac{dq_1}{dt} = -i_1 \quad (8)$$

$$\frac{dq_2}{dt} = i_2 \quad (9)$$

Such a system of equations can be easily solved by numerical methods. A computer program employing the fourth order Runge-Kutta method and the Adams-Moulton method is written for this purpose. Further details can be found in Appendices B and C. The boundary conditions are defined as follows:

$t < 0$, both S_1 and S_2 are opened.

$t = 0$, $\left\{ \begin{array}{l} S_1 \text{ closes and } S_2 \text{ remains opened.} \\ q_1 = Q = C_1 V_0 \quad (V_0 \text{ is the D.C. charging voltage}) \\ i_1 = i_2 = i_3 = q_2 = 0 \end{array} \right.$

$$t = t_0, \begin{cases} S_2 \text{ closes and } S_1 \text{ remains closed} \\ q_2 = Q - q_1 \\ i_1 = i_2 \\ i_3 = 0 \end{cases}$$

It is noted that t_0 is chosen so that $V_a(t_0)$ is the maximum voltage achievable (which is necessary for maximum power transfer). The other circuit parameters are defined as below unless otherwise specified:

$$\begin{array}{ll} C_1 = 10^{-7} \text{ F} & C_2 = 2.4 \times 10^{-8} \text{ F} \quad (d_w = 3.5 \text{ cm}) \\ R_1 = 1 \quad \Omega & L_1 = 66.7 \text{ nH} \\ R_0 = 0.4 \quad \Omega & L_0 = 36.45 \text{ nH} \\ R_L = 1 \quad \Omega & L_L = 0 \text{ nH} \\ \tau_R = 1 \quad \mu\text{s} & \tau_L = 0.5 \quad \mu\text{s} \end{array}$$

Two voltage measurements are of particular interest and they are $V_a(t)$ across the output ends of the transmission line and $V_b(t)$ across the dummy load resistor. These two voltage waveforms are calculated for $V_0 = -60 \text{ kV}$ and the effects of varying L_0 and τ_L are illustrated in Figures 19 and 20 respectively. Figure 19 shows that the current risetime (i.e. that of $V_b(t)$) and the energy delivery time is much smaller when L_0 is decreased from 50 nH to 10 nH. It can be seen from Figure 20 that the

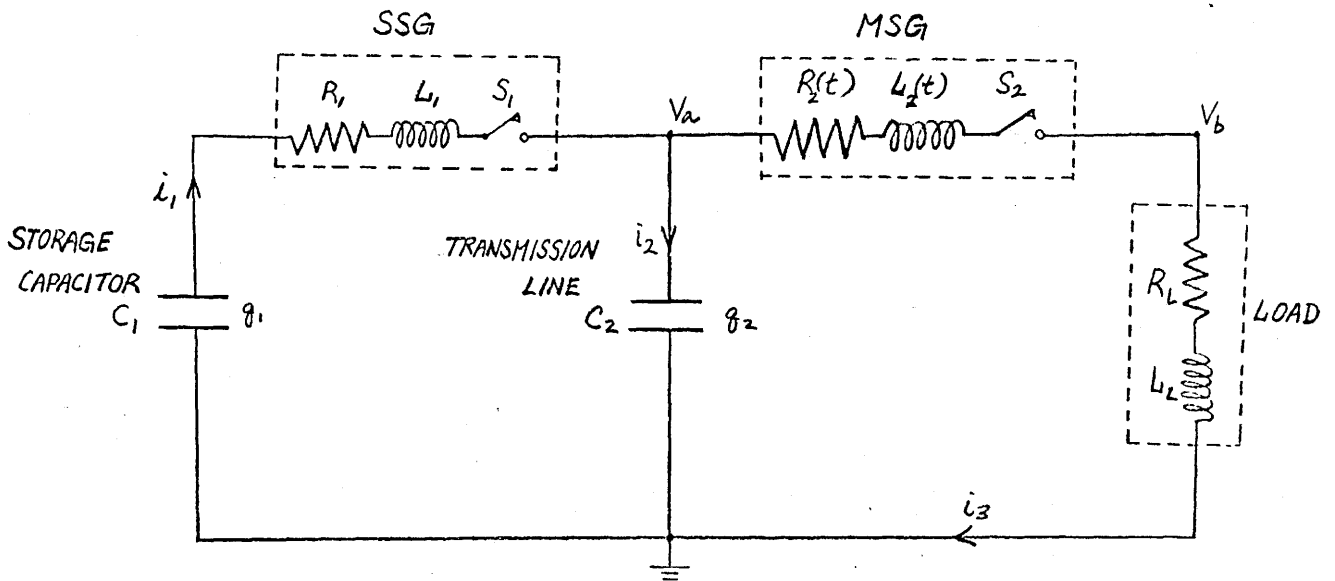


FIGURE 18(a) Equivalent Circuit of Resistive Load Assembly

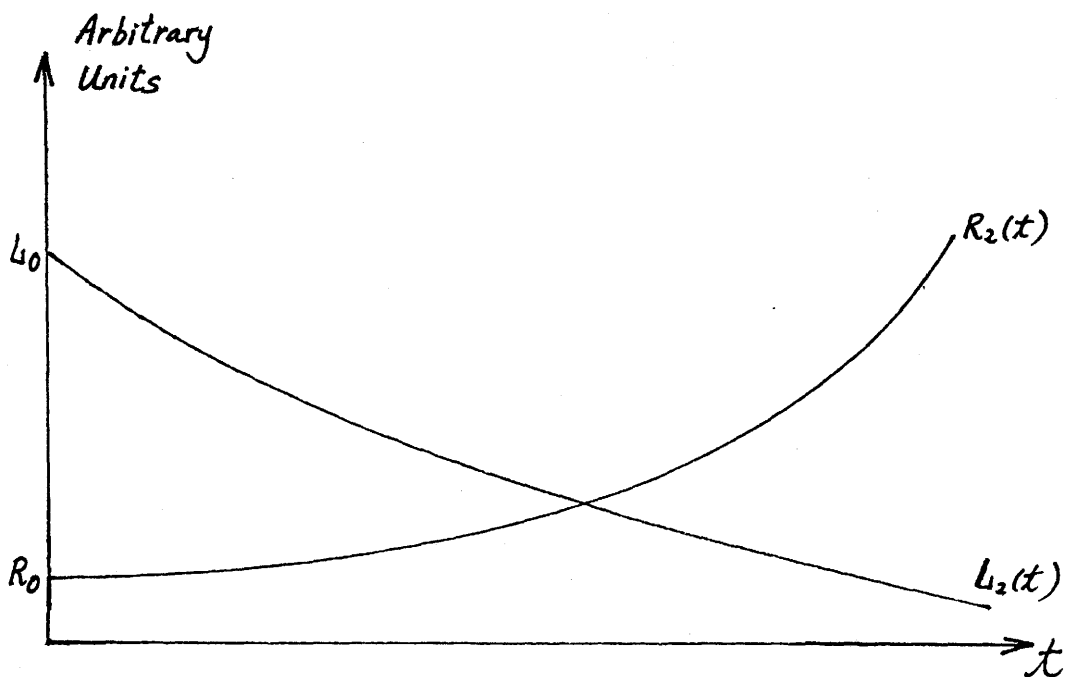


FIGURE 18(b) Assumed Time Function for R_2 and L_2

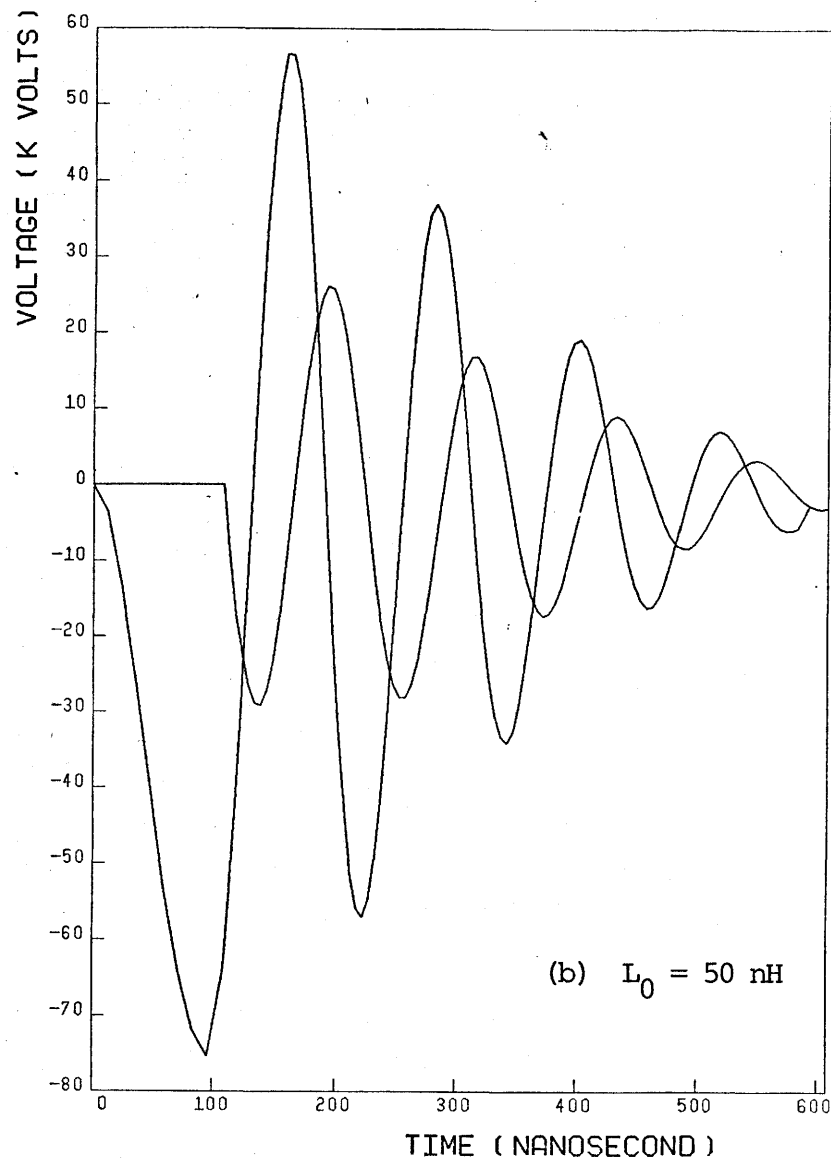
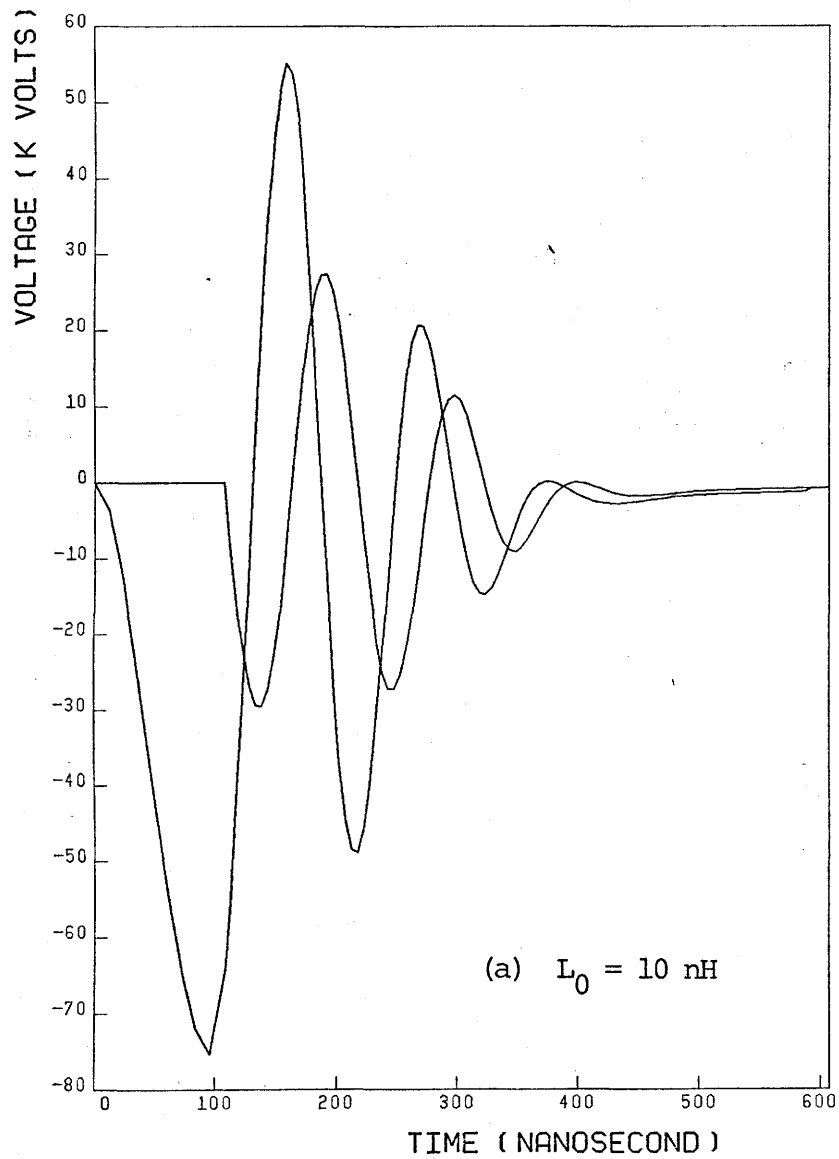


FIGURE 19 Effects of L_0 on Voltage and Current

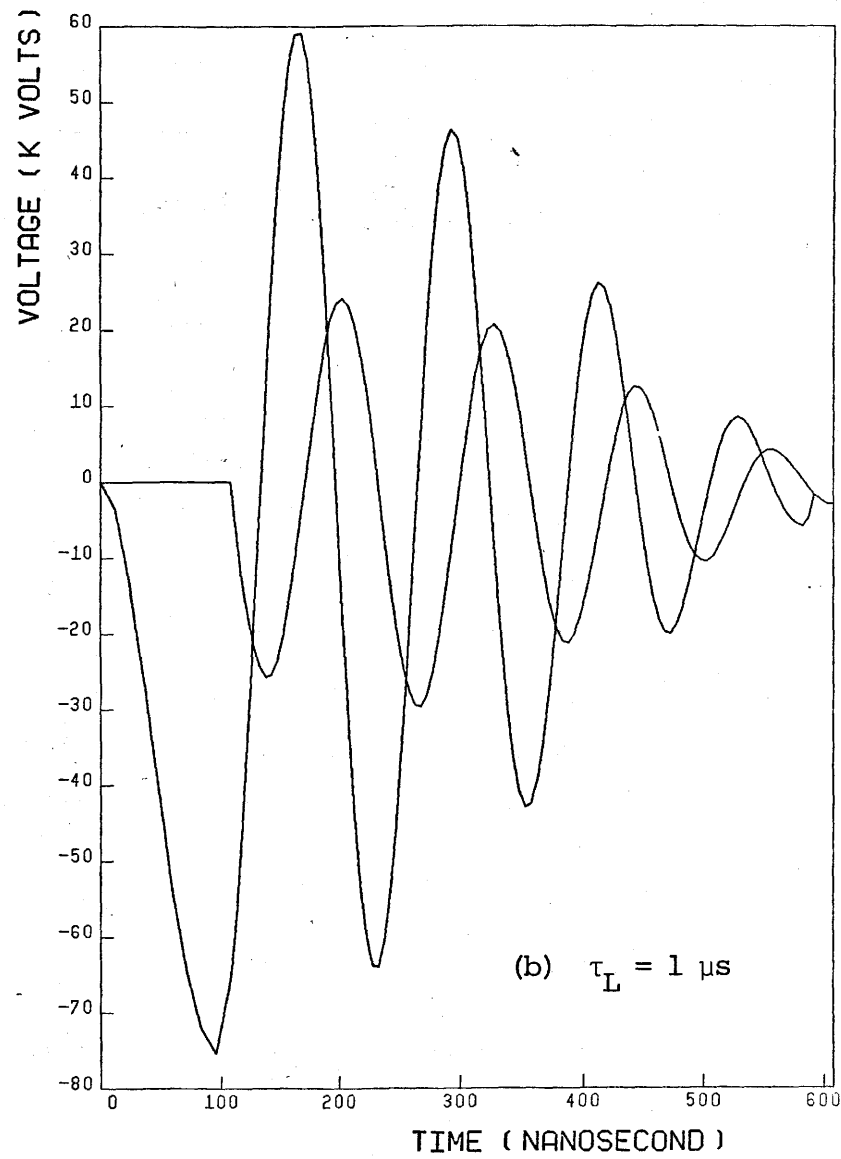
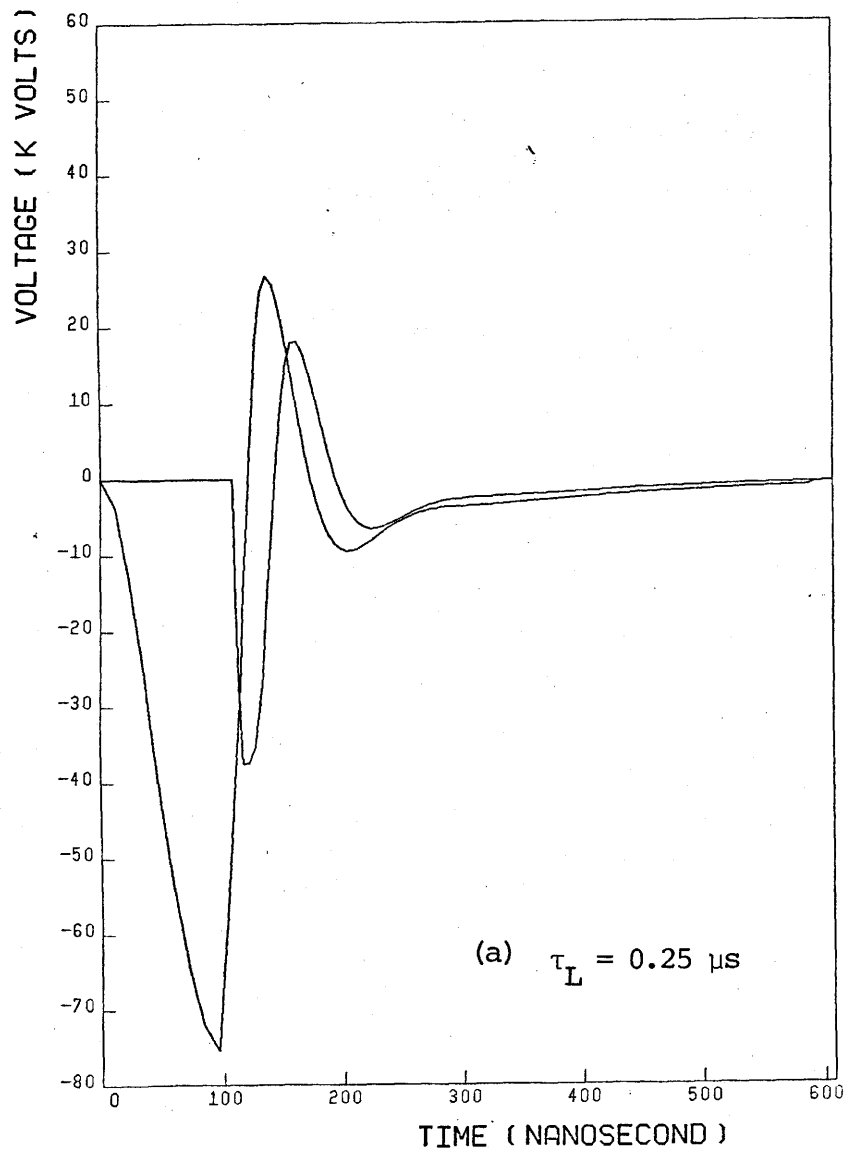


FIGURE 20 Effects of τ_L on Voltage and Current

e-folding time for $L_2(t)$ also has an effect on the damping of the voltages. The above calculations hence confirm the fact that a low inductance and a short inductive phase is desirable for switch design.

It is also noticed that the general shapes of the voltages calculated are quite similar to those observed in the experiments (see also Figures 14 and 16). This implies that the experimentally determined waveforms may be generated numerically with proper definitions of $L_2(t)$ and $R_2(t)$. However, this cannot be done in practice due to the infinite combinations of L_2 and R_2 that are possible. Nevertheless, the model is still quite useful in predicting qualitatively the effects on switch performance when one or more of the circuit parameters are being varied.

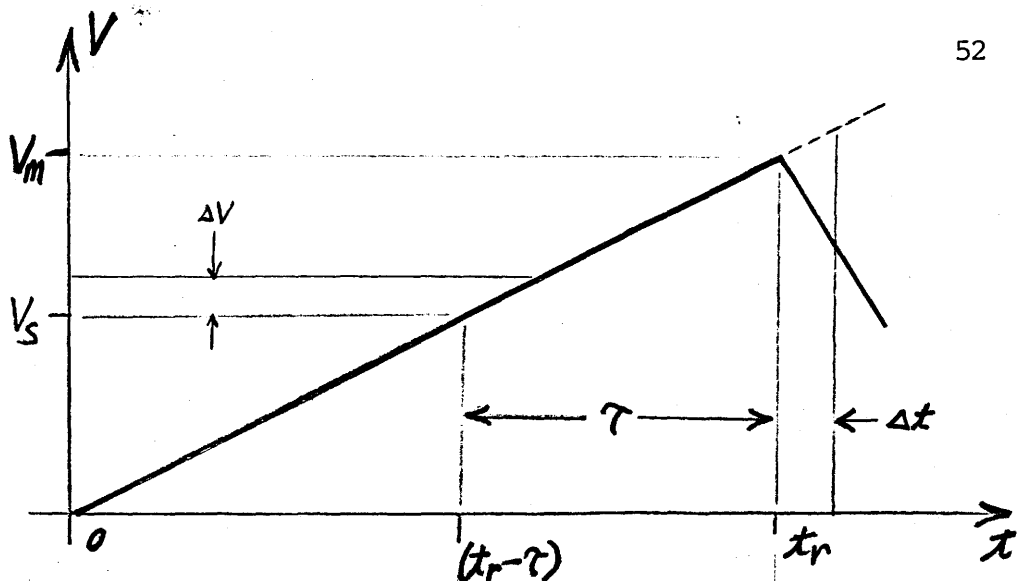
4.2 Physical Model

Unlike the engineering model, the physical model for the switch is to be derived from the basic theories of gas breakdown mechanisms. The present model covers only the holdoff phase of the breakdown process and takes into account of only a single channel. However, since the channel closure simultaneity of a multichannel switch is usually much smaller than the pulse charging time t_r , the model should apply equally well for the multichannel

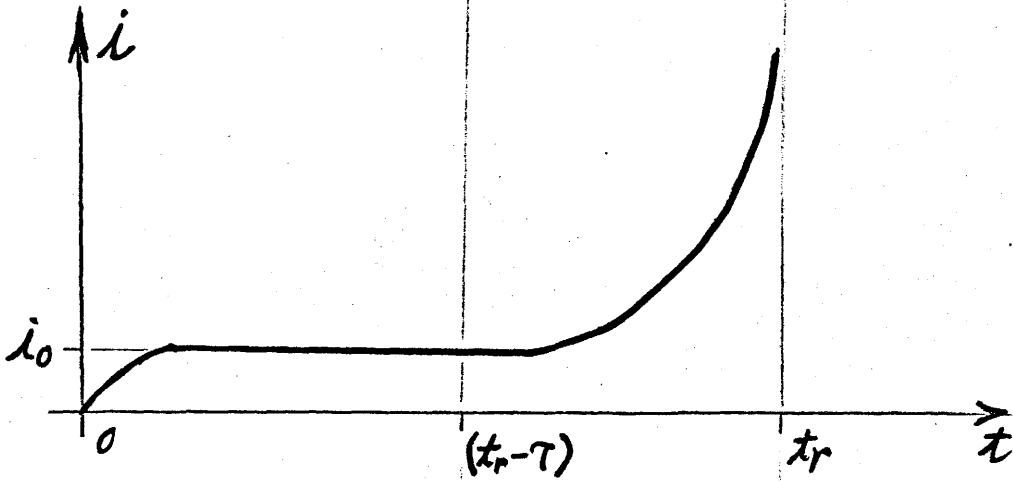
case.

Several different mechanisms of ion generation or loss are usually involved in an electrical discharge. These processes include (i) ion generation by electron collision, photoionization, positive ion collision, thermal ionization; and (ii) ion loss by attachment, recombination and diffusion, etc..⁽¹⁷⁾ Among these processes, ionization by electron impact is probably the most important process in gas breakdown and is assumed to be the only mechanism present in the derivation of this model.

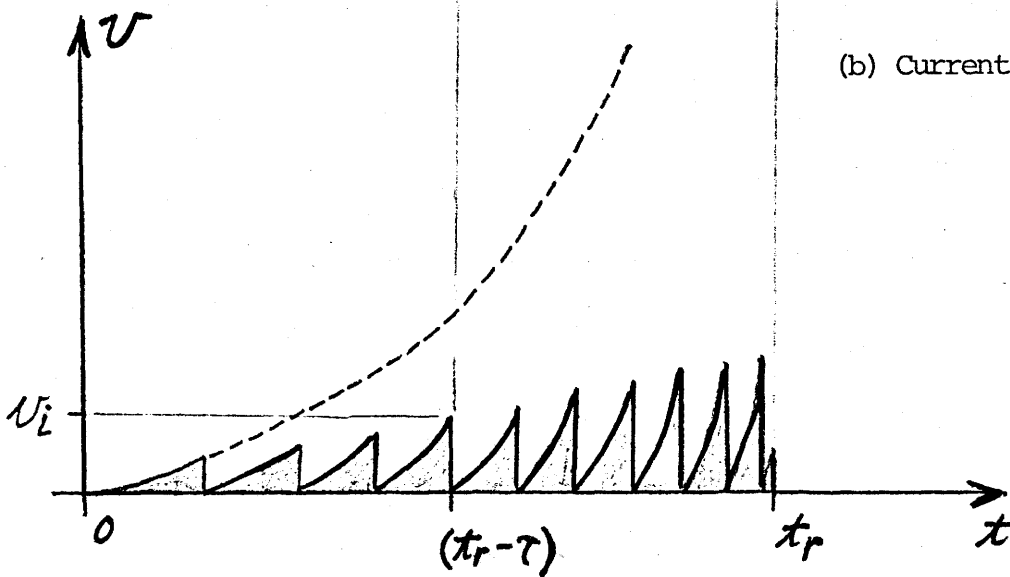
Figures 21(a) and 21(b) illustrate the current-voltage relationship in the pre-spark region as proposed by Townsend.⁽¹⁷⁾ It is assumed that the voltage is a linear function of time. The current in the gap increases slowly with the applied voltage at the beginning and then saturates at a value i_0 . The saturation occurs because the electrons and positive ions drift to the electrodes much faster than they can be replaced in the gas. If the voltage is increased beyond V_s , the current rises exponentially until a spark occurs. It is suggested by Townsend that the sudden increase in current is due to the ionization of gas by electron in a uniform field. The dotted line represents the velocity curve if there were no electron collision. In the



(a) Voltage



(b) Current



(c) Velocity of a Free Electron

FIGURE 21
Pre-Spark Characteristics

case with collisions, the electron will give up its kinetic energy to excite and/or to ionize the gas molecule. The collision is therefore an inelastic one and the electron velocity will drop to zero (at least approximately) after each collision. For voltages smaller than V_s , electrons do not gain enough kinetic energy between collisions to cause ionization of gas molecules. As the voltage increases, electrons are accelerated more and more between collisions until their velocity reaches v_i , the minimum velocity required to provide sufficient energy for ionization, and electron avalanche or multiplication may occur from then on. The voltage at which v_i is reached for the first time is denoted by V_s . It is obvious that V_s also corresponds to the static breakdown voltage of the gap (i.e. the minimum voltage for breakdown to occur). As the electrons are moving toward the anode, the positive ions generated by collisions are accelerated in the opposite direction. Emission of secondary electrons from the cathode may then be caused by the bombardment of these positive ions. Townsend's criterion for breakdown requires a new electron to be generated for every electron arriving at the anode and that the total number of electrons in the gap stays the same. The occurrence of secondary electrons would therefore quickly satisfy the above criterion and a self-sustaining discharge is obtained. The voltage at which breakdown occurs is denoted by V_m . Figure 21(b) indicates that current increases exponentially to infinity when breakdown occurs. In actual practice, the

size of the current is limited by external circuit parameters.

When a steady voltage greater than V_s is applied between a pair of electrodes, current does not start flowing immediately. The time elapses between the instant of application of the voltage and the appearance of an initial electron in the gap is called the statistical time lag (τ_s). Another time period is required for the initial electron to start the ionization process that leads to a self-sustaining discharge across the gap. This time period is called the formative time lag (τ_f). The sum of these two time lags is the total time lag τ . In the following derivation of the model, τ_s is assumed to be much smaller than τ_f so that τ is approximately equal to τ_f .⁽¹⁰⁾

According to the Townsend theory, the formative time lag depends mainly on the transit time of a positive ion from anode to cathode (electron transit time is negligible due to its higher mobility). However, it is found that the total time lag for breakdown at high pressure can be much less than the positive ion transit time. The discrepancy can be explained by the proposal of a streamer mechanism.⁽¹⁸⁾ The theory suggest that if the space charge produced by electron avalanche distorts the field sufficiently, auxiliary avalanches can be formed by photoionization in the space charge region. The positive space charge can therefore be extended rapidly toward the cathode to form a streamer. The entire process occurs

very fast and hence it can be assumed that the total time lag is equal to the time for an electron to travel from the cathode to the anode.

In Figure 21(c), each of the shaded areas represents the distance travelled by an electron between successive collisions and is assumed to be equal to a mean free path λ_m . The sum of the shaded areas within the time interval $(t_r - \tau, t_r)$ must therefore equal to the electrode separation d . The shaded areas can be approximated by perfect triangles as shown in Figure 22. An average velocity can then be defined for each time interval between collisions, Δt_j ,

$$\bar{v}(t_j) = \frac{v(t_j + \frac{\Delta t_j}{2})}{2} \quad (10)$$

where $j = 1, 2, 3, \dots, n$

For a linear charging rate,

$$V(t) = \frac{V_m}{t_r} t, \quad 0 \leq t \leq t_r \quad (11)$$

the electron acceleration is then given by

$$a(t) = \frac{e}{m} E(t) = \left(\frac{eV_m}{mdt_r} \right) t \quad (12)$$

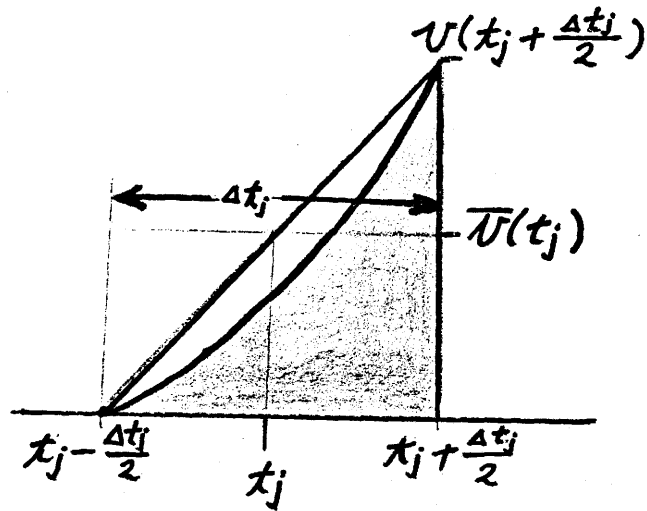


FIGURE 22

Notations used in Derivation of Model

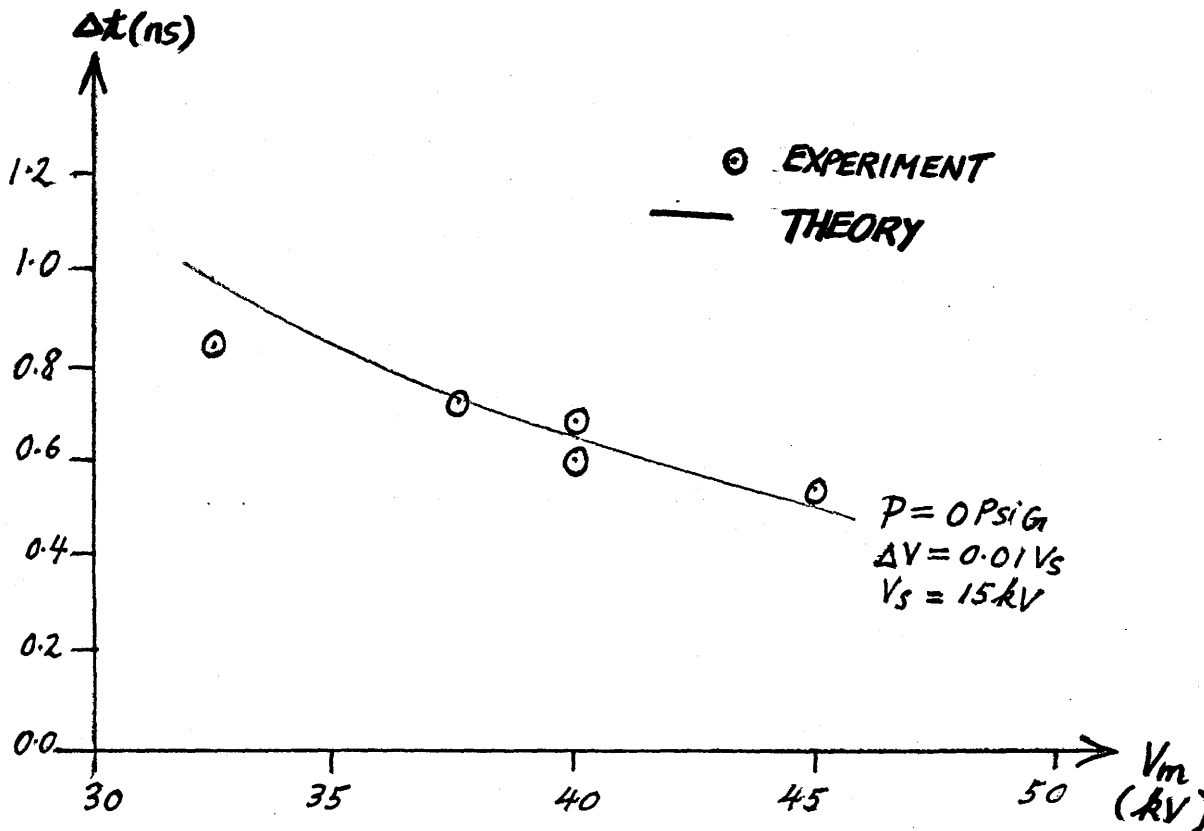


FIGURE 23

Jitter Time as a Function of Holdoff Voltage

where e is the electronic charge and

m is the rest mass of an electron.

But

$$v(t_j + \frac{\Delta t_j}{2}) = \int_{t_j - \frac{\Delta t_j}{2}}^{t_j + \frac{\Delta t_j}{2}} a(t) dt$$

Integrating gives,

$$v(t_j + \frac{\Delta t_j}{2}) = a(t_j) \frac{\lambda_m}{\bar{v}(t_j)} \quad (13)$$

Substituting into eq. (10) and rearranging terms,

$$\bar{v}(t_j) = \left[\frac{\lambda_m}{2} a(t_j) \right]^{1/2} \quad (14)$$

Now for $(t_r - \tau) < t < t_r$, $\Delta t_j \ll \tau$ and the following approximation can be made,

$$\sum_j \bar{v}(t_j) \Delta t_j \cong \int_{t_r - \tau}^{t_r} \bar{v}(t) dt \quad (15)$$

where \sum_j represents the summation of distances travelled between collisions in the time interval $(t_r - \tau, t_r)$.

From boundary condition,

$$\sum_j \bar{v}(t_j) \Delta t_j = d \quad (16)$$

Combining equations (12), (15), (16) and integrating,

$$\frac{2}{3} \left[\frac{\lambda_m}{2} \left(\frac{eV_m}{mdt_r} \right) \right]^{\frac{1}{2}} \left\{ t_r^{3/2} - (t_r - \tau)^{3/2} \right\} = d \quad (17)$$

An impulse ratio is defined as follows:

$$R = \frac{V_m}{V_s} = \left(\frac{t_r}{t_r - \tau} \right) \quad (18)$$

Substituting into eq.(17) obtains

$$\frac{2}{3} \left[\frac{\lambda_m}{2} \left(\frac{eV_m}{mdt_r} \right) \right]^{\frac{1}{2}} (1 - R^{-3/2}) t_r^{3/2} = d$$

Squaring both sides and rearranging terms,

$$V_m t_r^2 = \frac{9}{2} \frac{m d^3}{e \lambda_m (1 - R^{-3/2})^2} \quad (19)$$

Assuming that the $(1 - R^{-3/2})^2$ term is approximately a constant for a given gas pressure, then eq.(19) becomes,

$$V_m t_r^2 \cong \text{constant} = A \quad (20)$$

This appears to be in agreement with experiment results obtained before. (see Figure 12)

All of the parameters in equation (19) can be measured directly except λ_m . At one atm of nitrogen, V_s for the NRC switch was measured to be about 15 kV. Hence λ_m can be evaluated for atmospheric pressure using previous experiment results. The average value of λ_m thus obtained is 7.1×10^{-6} cm. This number appears to be a fairly reasonable one. The constant A in eq. (20) can also be determined and is found to be $1.2 \text{ kV-}\mu\text{s}^2$ for one atm of N_2 . In addition, since λ_m varies inversely with gas pressure, A is expected to increase as pressure rises. Figure 12 again confirms that this is the case: the slope of the straight lines increases with MSG pressure.

A formula for the jitter time can also be derived from eq. (19). Figure 19(a) gives the definition of Δt in terms of the voltage jitter ΔV :

$$\frac{\Delta t}{t_r} = \frac{\Delta V}{V_m} \quad (21)$$

Substituting eq. (19) into eq. (21) gives

$$\Delta t = \left[\frac{9}{2} \frac{m d^3}{e \lambda_m (1 - R^{-3/2})^2 V_m^3} \right]^{1/2} \Delta V \quad (22)$$

Figure 23 gives the calculated Δt for $P = 0$ PsiG. Once again, the theory fits the experimental results rather nicely.

The present model is no doubt an oversimplified one. In real practice, several mechanisms are taking place at the same time during the breakdown process and more complicated theories must therefore be employed to describe the phenomena in detail. However, this elementary model is quite capable in predicting some of the results observed in the experiments.

CHAPTER 5

CONCLUSIONS

5.1 Summary of Results

The effects of the presence of a dielectric surface is studied in two different cases. For the single channel D.C. case, the dielectric has been shown to lower the static breakdown voltage in air considerably when it is placed at a small distance away from the electrodes. In the pulse breakdown case, it is found that the dielectric surface enhanced multichanneling in a long gap. It is believed that these two effects may be related directly to each other with better understanding of the surface discharge phenomena. An attempt of establishing dependences of experimental data on material properties in the static case turns out to be a failure. No definite conclusions can be drawn from the measurements although some general trends are still observed. However, this does not mean that surface discharge does not depend on these material properties but rather that a number of processes are involved at the same time. These processes all contribute to determine the external field and the resulting field configuration is a complicated one. The establishment of dependence on a single process is therefore extremely

difficult if not at all impossible.

The NRC switch is used to study the effects of V_0 on V_m , t_r and N for different gas pressures. The relationship between V_m and t_r is also noted. These results have indicated that a high D.C. charging voltage and an appropriate choice of P is essential for intense multichanneling with high holdoff voltages. The measurement of $Z(t)$ has provided another method of characterizing the switch. Furthermore, the switch closing period can be determined from the duration of the light output as detected by a fast photodetector.

Lifetime of the switch is studied in terms of surface erosion and performance degradation. Quartz is found to be the best among the dielectric samples examined in both categories. However, for extending the lifetime into 10^7 shots, insulating material with a still higher melting point than quartz is required. In addition, it may also be necessary to separate the dielectric and the electrodes by a small distance so that damage can be reduced without significantly affecting the switch performance.

An engineering model which treats the MSG as a resistor and an inductor in series is presented. While the measured $Z(t)$ and the

detected light output may provide an estimate for $R(t)$ and $L(t)$, the exact form for these quantities cannot be defined. The model is therefore not very useful in its present form. However, it does suggest that a low inductance value and a short inductive phase are desirable. Finally, a physical model derived from gas breakdown theory predicts that $V_m t_r^2$ is approximately a constant. This relationship is observed experimentally with the NRC switch. The mean free path of collision is determined to be 7.1×10^{-6} cm at one atm of N_2 . The constant A should be as large as possible for providing both a high holdoff voltage and a slow charging rate. The model predicts that high pressure operation of the switch is desirable for this purpose. Experiment results seem to confirm this fact. A formula for jitter time is derived and Δt is evaluated for $\Delta V = 0.01 V_s$. Again, experiment results are in good agreement with theory.

5.2 Suggestions for Future Investigation

The present study has provided an insight into the surface discharge switches. However, for optimum design and efficient operation of the switches, further investigation is necessary. The following areas should be examined in the future:

(A) Gaining better understanding of surface discharge physics, both in static and in pulse breakdown cases.

- (B) Extending lifetime of switch by looking for new materials and by finding an optimum separation between dielectric surface and electrodes.
- (C) Attempting to define $R(t)$ and $L(t)$ explicitly.
- (D) Measuring V_g at higher pressures so that the physical model can be further tested.
- (E) Developing a physical model for the energy delivery phase.

The above listed studies are thought to be essential for improving the switch design.

APPENDIX A
LIST OF EQUIPMENT

<u>Component</u>	<u>Company</u>	<u>Model</u>	<u>Feature</u>
Power Supply	Universal Voltronics	BAL-100-2-M	{ 0-100 kV 0-2 mamp
Storage Capacitor	Maxwell		0.1 μ F
Single Spark Gap	Physics International	670	60 nH
Oscilloscope	Tektronix Inc.	{ 7834 545 A	
Photodetector	Opto-electronics Ltd.	PD 10	100 psec risetime

APPENDIX B
 NUMERICAL METHODS

A p th order differential equation can be expressed as a system of p first order differential equations. Let Σy_j represents the sequence $(y_1, y_2, y_3, \dots, y_p)$. Then each of the p equations would assume the following form:

$$y_j' = f_j(t, y_1, y_2, y_3, \dots, y_p) = f_j(t, \Sigma y_j)$$

where $1 \leq j \leq p$ and j is an integer.

Let $y_{j,n} = y_j(t_n)$ and Runge-Kutta method of the order four gives:

$$y_{j,n+1} = y_{j,n} + \frac{1}{6} (A_j + 2B_j + 2C_j + D_j)$$

$$\text{where } \begin{cases} A_j = h f_j(t_n, \Sigma y_{j,n}) \\ B_j = h f_j(t_n + \frac{h}{2}, \Sigma(y_{j,n} + \frac{A_j}{2})) \\ C_j = h f_j(t_n + \frac{h}{2}, \Sigma(y_{j,n} + \frac{B_j}{2})) \\ D_j = h f_j(t_n + h, \Sigma(y_{j,n} + \frac{C_j}{2})) \end{cases}$$

and $h = t_{n+1} - t_n$

The above method is a self-starting one (i.e. $y_{j,n+1}$ depends only on the previous value of $y_{j,n}$) but is rather time consuming since f_j has to be evaluated four times for each time step. Another method, the Adams-Moulton method, is therefore chosen to minimize the computing time. Since the latter method is not self-starting, Runge-Kutta method is employed for the evaluation of the initial four values of y_j and the Adams-Moulton method is then used to carry on calculating the remaining values. The recurrence relation for the latter is defined as below:

$$y_{j,n+1} = y_{j,n} + \frac{h}{24} \left\{ 55 f_j(t_n, \Sigma y_{j,n+1}) - 59 f_j(t_{n-1}, \Sigma y_{j,n-1}) \right. \\ \left. + 37 f_j(t_{n-2}, \Sigma y_{j,n-2}) - 9 f_j(t_{n-3}, \Sigma y_{j,n-3}) \right\}$$

$$y_{j,n+1} = y_{j,n} + \frac{h}{24} \left\{ 9 f_j(t_{n+1}, \Sigma y_{j,n+1}) + 19 f_j(t_n, \Sigma y_{j,n}) \right. \\ \left. - 5 f_j(t_{n-1}, \Sigma y_{j,n-1}) + f_j(t_{n-2}, \Sigma y_{j,n-2}) \right\}$$

It can be seen that the Adams-Moulton method is faster because only two evaluations of the derivative f_j is necessary in most cases.

APPENDIX C

COMPUTER PROGRAM LISTING

```

C      PROGRAM CIRCUIT (INPUT,OUTPUT)
C      COMMON D(10),VAR(10,100),Y(10),DER(10),TEMP(10,4),X0,XS,H,
+      NVAR,NVAR1,NSTEP,NSTEP1,NDATA,NDATA1
COMMON /B1/ R,R1,L,L1,C1,C2,C,VS,ALPHA,OMG,ANGLE,ESL,T,T0,TR,
+      TL,R0,L0,Q
+      REAL R,R1,L,L1,C1,C2,ANGLE,ALPHA,OMG,ESL,Q,VS,T0,C,T,TR,TL,R0,
+      L0,LP,RP
REAL POINTX(200),POINTY(200)
REAL D,VAR,Y,YP,DER,TEMP,X0,XS,H
INTEGER NDATA,NVAR,NSTEP

C      C
C      C
C      C      INITIALIZATION
10     READ 10,NVAR,NDATA,H
      FORMAT (2I10,E10.5)
      NVAR1=NVAR+1
      NDATA1=NDATA+1
      DO 20 I=1,NDATA
20     READ 30,D(I)
30     FORMAT (E10.5)
      CALL BOUND
      NSTEP=IFIX((XS-X0)/H)+1
      NSTEP1=NSTEP+1

C      C
C      C      CALCULATE FIRST 4 POINTS BY RUNGE-KJTTA METHOD.
100    DO 100 I=1,NVAR1
      Y(I)=VAR(I,1)
      CALL DVAR
110    DO 110 I=1,NVAR
      TEMP(I,1)=DER(I)
      CALL RUKU

C      C
C      C      CALCULATE REMAINING POINTS BY ADAMS-MOULTON METHOD.
      CALL ADMO

C      C
C      C      OUTPUT PLOT.
      Y0=-80000.
      YS=60000.
      CALL READY (X0,XS,Y0,YS)
      DO 120 J=1,9
120    POINTY(J)=0.
      POINTX(J)=(J-1)*T0*1.E9/9.
      DO 150 J=1,NSTEP1
150    POINTX(J+9)=(VAR(1,J)+T0)*1.E9
      POINTY(J+9)=(VAR(2,J)-VAR(3,J))*D(6)
      NPLOT=NSTEP1+9
      CALL CURVE (POINTX,POINTY,NPLOT)
      DO 155 J=1,9
155    T=POINTX(J)*1.E-9
      POINTY(J)=Q*(1.-(EXP(-ALPHA*T)*SIN(OMG*T+ESL))/ANGLE)/C2
      DO 160 J=4,NSTEP
      RP=R1+R0*EXP(VAR(1,J)/TR)
      LP=L1+L0*EXP(-VAR(1,J)/TL)
160    POINTY(J+6)=((VAR(2,J+1)-VAR(3,J+1))-
+      (VAR(2,J)-VAR(3,J)))
      /H*LP+(VAR(2,J)-VAR(3,J))*RP
      NPLOT=NSTEP1+6
      CALL CURVE (POINTX,POINTY,NPLOT)
      CALL PLOT (.1,-1,-3)
      CALL PLOT (0.,0.,999)

C      C
      STOP
      END

```

```

SUBROUTINE ADMO
C
COMMON D(10),VAR(10,100),Y(10),DER(10),TEMP(10,4),X0,XS,H,
+ NVAR,NVAR1,NSTEP,NSTEP1,NDATA,NDATA1
REAL D,VAR,Y,YP,DER,TEMP,X0,XS,H
INTEGER NDATA,NVAR,NSTEP
C
NITEP=3
DO 200 J=4,NSTEP1
DO 120 I=2,NVAR1
Y(I)=VAR(I,J)+H/24.*(55.*TEMP(I-1,4)-59.*TEMP(I-1,3)+37.*
+ TEMP(I-1,2)-9.*TEMP(I-1,1))
120 CONTINUE
Y(1)=VAR(1,J)+H
DO 160 K=1,NITER
CALL DVAR
DO 150 I=2,NVAR1
150 VAR(I,J+1)=VAR(I,J)+H/24.*(9.*DER(I-1)+19.*TEMP(I-1,4)-5.*
+ TEMP(I-1,3)+TEMP(I-1,2))
VAR(1,J+1)=VAR(1,J)+H
DO 155 I=1,NVAR1
155 Y(I)=VAR(I,J)
160 CONTINUE
CALL DVAR
DO 180 I=1,NVAR
TEMP(I,1)=TEMP(I,2)
TEMP(I,2)=TEMP(I,3)
TEMP(I,3)=TEMP(I,4)
TEMP(I,4)=DER(I)
180 CONTINUE
200 CONTINUE
C
RETURN
END

SUBROUTINE BOUND
C
COMMON D(10),VAR(10,100),Y(10),DER(10),TEMP(10,4),X0,XS,H,
+ NVAR,NVAR1,NSTEP,NSTEP1,NDATA,NDATA1
COMMON /B1/ R,R1,L,L1,C1,C2,C,VS,ALPHA,OMG,ANGLE,ESL,T,T0,TR,
+ TL,RO,LO,Q
REAL R,R1,L,L1,C1,C2,ANGLE,ALPHA,OMG,ESL,Q,VS,T0,C,T,TR,TL,RO,
+ LO,LP,RP
C
REAL D,VAR,Y,YP,DER,TEMP,X0,XS,H
INTEGER NDATA,NVAR,NSTEP
C
RO=0.4
TR=1.E-6
LO=3.645E-8
TL=0.5E-6
X0=D(1)
XS=D(2)
C1=D(3)
C2=5.9E-8/D(4)
R=D(5)
R1=D(6)
L=D(7)
L1=D(8)
VS=D(9)
C=(C1*C2)/(C1+C2)
ALPHA=R/2.0/L
OMG=SQRT(1.0/L/C-ALPHA**2)
ANGLE=OMG/SQRT(OMG**2+ALPHA**2)
ESL=ASIN(ANGLE)
T0=(1.5*3.14159-ESL)/OMG
Q=C*VS
VAR(1,1)=X0
VAR(2,1)=Q*(OMG/ANGLE**2)*EXP(-ALPHA*T0)*SIN(OMG*T0)
VAR(3,1)=VAR(2,1)
VAR(5,1)=Q*(1-EXP(-ALPHA*T0)*SIN(OMG*T0+ESL))/ANGLE)
VAR(4,1)=Q-VAR(5,1)
C
PRINT 20, C1,C2,C,R,R1,L,L1,VS,OMG,ANGLE,ESL,T0,Q,XS
20 FORMAT ( " C1= ",E10.2//
+ " C2= ",E10.2//
+ " C = ",E10.2//
+ " R = ",E10.2//
+ " R1= ",E10.2//
+ " L = ",E10.2//
+ " L1= ",E10.2//
+ " VS= ",E10.2//
+ " OMG= ",E10.2//
+ " ANGLE= ",E10.2//
+ " ESL = ",E10.2//
+ " T0= ",E10.2//
+ " Q = ",E10.2//
+ " XS= ",E10.2// )
C
PRINT 30, VAR(2,1),VAR(3,1),VAR(4,1),VAR(5,1)
30 FORMAT ( " I1 = ",E10.2//
+ " I2 = ",E10.2//
+ " Q1 = ",E10.2//
+ " Q2 = ",E10.2// )
C
RETURN
END

```

```

SUBROUTINE CURVE (POINTX,POINTY,N)
REAL POINTX(200),POINTY(200)
N1=N-1
CALL NEWPEN (2)
DO 1000 I=1,N1
CALL PLTLN (POINTX(I),POINTY(I),POINTX(I+1),POINTY(I+1))
CONTINUE
RETURN
END
1000

```

```

SUBROUTINE DVAR
C
COMMON D(10),VAR(10,100),Y(10),DER(10),TEMP(10,4),X0,XS,H,
+ NVAR,NVAR1,NSTEP,NSTEP1,NDATA,NDATA1
COMMON /B1/ R,R1,L,L1,C1,C2,C,VS,ALPHA,OMG,ANGLE,ESL,T,T0,TR,
+ TL,RO,LO,Q
REAL R,R1,L,L1,C1,C2,ANGLE,ALPHA,OMG,ESL,Q,VS,T0,C,T,TR,TL,RO,
+ LC,LP,RP
REAL D,VAR,Y,YP,DER,TEMP,X0,XS,H
INTEGER NDATA,NVAR,NSTEP
C
RP=R1+RO*EXP(Y(1)/TR)
LP=L1+LO*EXP(-Y(1)/TL)
DER(1)=-1./L*(R*Y(2)+Y(4)/C1+Y(5)/C2)
DER(2)=-((LP*R-L*RP)*Y(2)+L*RP*Y(3)+(LP/C1)*Y(4)+((LP+L)/C2)*Y(5))
+ /((L*LP)
DER(3)=Y(2)
DER(4)=Y(3)
C
RETURN
END

```

```

SUBROUTINE RUKU
C
COMMON D(10),VAR(10,100),Y(10),DER(10),TEMP(10,4),X0,XS,H,
+ NVAR,NVAR1,NSTEP,NSTEP1,NDATA,NDATA1
REAL K1(10),K2(10),K3(10),K4(10)
REAL D,VAR,Y,YP,DER,TEMP,X0,XS,H
INTEGER NDATA,NVAR,NSTEP
C
DO 200 J=1,3
DO 60 I=1,NVAR
60 K1(I)=DER(I)*H
Y(1)=VAR(1,J)+H/2.0
DO 70 I=2,NVAR1
70 Y(I)=VAR(I,J)+K1(I-1)/2.0
CALL DVAR
DO 80 I=1,NVAR
80 K2(I)=DER(I)*H
DO 90 I=2,NVAR1
90 Y(I)=VAR(I,J)+K2(I-1)/2.0
CALL DVAR
DO 100 I=1,NVAR
100 K3(I)=DER(I)*H
Y(1)=VAR(1,J)+H
DO 110 I=2,NVAR1
110 Y(I)=VAR(I,J)+K3(I-1)
CALL DVAR
DO 120 I=1,NVAR
120 K4(I)=DER(I)*H
DO 130 I=1,NVAR
130 VAR(I+1,J+1)=VAR(I+1,J)+1./6.*(K1(I)+2.*K2(I)+2.*K3(I)+K4(I))
CONTINUE
VAR(1,J+1)=VAR(1,J)+H
DO 150 I=1,NVAR1
150 Y(I)=VAR(I,J)
CALL DVAR
DO 160 I=1,NVAR
160 TEMP(I,J+1)=DER(I)
200 CONTINUE
C
RETURN
END

```

```

SUBROUTINE READY (X0,XS,Y0,YS)
*****
THIS SUBROUTINE PLOTS THE AXIS LABEL AND THE BORDER LINE.
*****
COMMON /B1/ R,R1,L,L1,C1,C2,C,VS,ALPHA,OMG,ANGLE,ESL,T,TO,TR,
+ TL,RO,LO,0
REAL R,R1,L,L1,C1,C2,ANGLE,ALPHA,OMG,ESL,Q,VS,TO,C,T,TR,TL,RO,
+ LC,LP,RP
REAL TEMPX(2),TEMPY(2)
TEMPX(1)=XC*1.E9
TEMPX(2)=(XS+T0)*1.E9
TEMPY(1)=Y0
TEMPY(2)=YS
PRINT*, TEMPX(1),TEMPX(2),TEMPY(1),TEMPY(2)

DRAW OUTER LIMIT OF PLOTTING AREA WITH WIDE LINE.
CALL NEWPEN(9)
CALL PLOT (0.,0.02,3)
CALL PLOT (0.,10.535,2)
CALL PLOT (0.,0.02,2)

SCALE DATA TO ALLOW ONE INCH MARGIN ALL AROUND.
CALL FACTOR (2,TEMPX,TEMPY,7.0,9.555,1.0,1.0)

DETERMINE MIN. AND MAX. VALUES OF DATA AND
DRAW BORDER USING NORMAL LINE WIDTH.
CALL NEWPEN (1)
CALL INCHTO (1.0,1.0,XMN,VMN)
CALL INCHTO (7.0,9.555,XXM,VMX)

CALL PLTLN (XMN,VMN,XMN,VMX)
CALL PLTLN (XMN,VMX,XXM,VMX)
CALL PLTLN (XXM,VMX,XXM,VMN)
CALL PLTLN (XXM,VMN,XMN,VMN)

PLOT DIVISIONS ON X AXIS.
NX=INT((TEMPX(2)-TEMPX(1))/100.)+1
X1=0.85
HX=.1
DO 900 I=1,NX
CALL PLOT (X1+0.15,1.0,3)
CALL PLOT (X1+0.15,1.1,2)
IWS0=(I-1)*100.
ENCODE (3,850,XSCALE) IWS0
FORMAT (I3)
CALL LETTER (3,HX,0.0,X1,.85,XSCALE)
X1=X1+60./(TEMPX(2)-TEMPX(1)) *10.
CONTINUE

PLOT DIVISIONS ON Y AXIS.

NY=INT((TEMPY(2)-TEMPY(1))/10000.)+1
Y1=1.0
HY=.1
DO 1000 I=1,NY
CALL PLOT (1.0,Y1,3)
CALL PLOT (1.1,Y1,2)
IWS1=(I-1+INT(TEMPY(1)/10000.))*10
ENCODE (3,850,YSCALE) IWS1
CALL LETTER (3,HY,0.0,.65,Y1,YSCALE)
Y1=Y1+85.55/(TEMPY(2)-TEMPY(1)) *1000.
CONTINUE

PLOT X AXIS LABEL.
CALL NEWPEN(4)
CALL LETTER (19,.15,0.0,3.40,0.50," TIME (NANOSECOND) ")

PLOT Y AXIS LABEL.
CALL LETTER (18,.15,90...50,7.0," VOLTAGE (K VOLTS) ")

RETURN
END

```

REFERENCES

1. W.J. Sarjeant, A.J. Alcock and K.E. Leopold, " A Scalable Multiatmosphere High-Power XeF Laser ", Applied Physics Letters, 30, p.635 (1977).
2. W.J. Sarjeant, A.J. Alcock and K.E. Leopold, " Parametric Study of a Constant E/N Pumped High-Power KrF Laser ", IEEE Journal of Quantum Electronics, QE-14, p.177 (1978).
3. R.S. Taylor, W.J. Sarjeant, A.J. Alcock and K.E. Leopold, "Glow-Discharge Characteristics of 0.8 J Multiatmosphere Rare Gas Halide Laser ", Optics Communication, 25, p.231 (1978).
4. R. Burnham, " Ultraviolet-Preionized Discharge-Pumped Lasers in XeF, KrF and ArF ", Applied Physics Letters, 29, p.707 (1976).
5. W.J. Sarjeant, R.S. Taylor, A.J. Alcock and K.E. Leopold, " Multichannel Surface Spark Gaps ", IEEE Transactions on Electron Devices, ED-26, p.1401 (1979)

6. T.R. Burkes, J.P. Craig, H.O. Hagler, M. Kristiansen, and W.M. Portnoy, " A Review of High-Power Switch Technology ", IEEE Transactions on Electron Devices, ED-26, p.1401 (1979).
7. Private Communication from Dr. S.T. Pai : " The Formation of Discharge Over Dielectric Surfaces ", Opto-Electronics Report, May 1980.
8. L.L. Alston, " Field Sketching ", High-Voltage Technology, L.L. Alston, ed., Oxford University Press, p.8 (1968).
9. W.J. Sarjeant, " High-Pressure Surface-Discharge Plasma Switches ", IEEE Transactions on Plasma Science, PS-8, p.216 (1980).
10. J.C. Martin, "Nanosecond Pulse Techniques ", AWRE SSWA/JCM/704/49, 1970.
11. W.J. Sarjeant and A.J. Alcock, " High-Voltage Probe System with Subnanosecond Risetime ", Review of Scientific Instruments, 47, p.1283 (1972).
12. A.J. Schwab, High-Voltage Measurement Techniques, The MIT Press, 1972.

13. R.S. Taylor, A.J. Alcock and K.E. Leopold, " Electrical and Gain Characteristics of a simple Compact XeCl laser ", Optics Communications, 31, p.197 (1979).
14. Private Communication from Dr. S.T. Pai and Dr. J.P. Marton : " Multichannel Surface Discharge in Pulse Charged Spark Gaps ", Opto-Electronics Report, Aug. 1980.
15. Private Communication from Dr. S.T. Pai : " Circuit Analysis of Multichannel Spark Gap Switch with Power Source and Laser Load ", Opto-Electronics Report, Mar. 1980.
16. R. Burnham, " Efficient Electric Discharge Lasers in XeF and KrF ", Applied Physics Letters, 29, p.30 (1976).
17. E. Kuffel and M. Abdullah, High Voltage Engineering, Pergamon Press, New York, 1970.
18. A.M. Howatson, An Introduction to Gas Discharges, 2nd ed., Pergamon Press, 1976.
19. S.D. Conte and C. de Boor, Elementary Numerical Analysis, 2nd ed., McGraw-Hill, 1972.